# Probing the impact of UV radiation on the isotopic chemistry in the outflow of AGB stars

Marte Cecilie Wegger

# Abstract

Low- and intermediate-mass stars ($0.8$-$8\,\mathrm{M}_\odot$) lose mass in a late stage of their evolution, called the asymptotic giant branch (AGB) phase. The mass and dust ejected into space enriches the interstellar medium and creates a circumstellar envelope (CSE) around the AGB star. We want to study CSEs in order to gain a better understanding of their chemical composition, but they are challenging to model precisely. The $^{12}\mathrm{CO}/^{13}\mathrm{CO}$ isotopologue ratio in CSEs has been used as a tracer for the photospheric $^{12}\mathrm{C}/^{13}\mathrm{C}$ ratio in CSEs, which is a good tracer of the stellar nucleosynthesis, but it might not be a reliable tracer for the $^{12}\mathrm{C}/^{13}\mathrm{C}$ ratio in UV irradiated regions as it is affected by UV radiation. We want to test if the $\mathrm{H}^{12}\mathrm{CN}/\mathrm{H}^{13}\mathrm{CN}$ abundance ratio, a ratio which is not affected by UV radiation, is a better tracer for the $^{12}\mathrm{C}/^{13}\mathrm{C}$ ratio than the $^{12}\mathrm{CO}/^{13}\mathrm{CO}$ ratio. In this thesis, we model CSEs for two UV active AGB stars, W Hydrae and R Leporis. We perform radiative transfer analysis of observed rotational transitions for $\mathrm{H}^{12}\mathrm{CN}$ and $\mathrm{H}^{13}\mathrm{CN}$ lines by use of accelerated lambda iterations, fit the observed data to the calculated models, and measure the $\mathrm{H}^{12}\mathrm{CN}/\mathrm{H}^{13}\mathrm{CN}$ isotopologue ratios using initial abundance values provided from a good fit between model and data. For carbon-rich R Leporis, we find that the $\mathrm{H}^{12}\mathrm{CN}/\mathrm{H}^{13}\mathrm{CN}$ abundance ratio is consistent with the previously reported $^{12}\mathrm{C}/^{13}\mathrm{C}$ ratio and show a small discrepancy with the previously reported $^{12}\mathrm{CO}/^{13}\mathrm{CO}$ ratio. This result suggests that the $\mathrm{H}^{12}\mathrm{CN}/\mathrm{H}^{13}\mathrm{CN}$ ratio can be a more reliable tracer for the C ratio in UV dominated CSEs for carbon-rich AGB stars than the previous commonly used CO ratio. For oxygen-rich W Hydrae, our analysis predicts an $\mathrm{H}^{12}\mathrm{CN}/\mathrm{H}^{13}\mathrm{CN}$ ratio consistent with the previously reported $^{12}\mathrm{C}/^{13}\mathrm{C}$ and $^{12}\mathrm{CO}/^{13}\mathrm{CO}$ ratios. In future work, we suggest observing several oxygen-rich UV active AGB stars and creating a larger sample of HCN ratios. By looking at the overall trend in the comparison between HCN ratios and CO and C ratios, we hope to increase our understanding of the impact of UV radiation on the isotopic chemistry in CSEs for oxygen-rich AGB stars.

# Acknowledgments

First, I want to give a huge thank you to my supervisors Maryam Saberi and Sven Wedemeyer. Thank you both for encouraging me, for your guidance and patience, for helping me understand when I felt lost, and for including me in the excellent research environment at ITA and in the solar/stellar group. I am grateful to have been a small part of this. I want to especially thank Maryam, who has offered fantastic support during this project, answering my questions and always being available on either chat, zoom or in person for discussion.

I also want to thank my family and friends, especially my parents, for the support and encouragement they have given me during this time. Thanks to my fellow stellar cellar students for long lunch breaks filled with interesting conversations. A special thanks to Olav, my clever brother-in-law, for proofreading this thesis. And last but not least, I want to thank my friends Maria and Kaspara for being by my side since day one at Blindern, for helping me, for making me laugh and for reminding me that school is not everything.

Thank you all, I honestly don't think I could have done this without you.

# Contents

# Acronyms

**AGB**: Asymptotic Giant Branch
**ALI**: Accelerated Lambda Iteration program
**ALMA**: Atacama Large Milimeter/submillimeter Array
**APEX**: Atacama Pathfinder EXperiment
**C**: Carbon
**CLASS**: Continuum and Line Analysis Single-dish Software
**CNO**: Carbon-nitrogen-oxygen
**CO**: Carbon monoxide
**CoG**: Curve-of-growth
**CSE**: Circumstellar envelope
**E-AGB**: Early Asymptotic Giant Branch
**GALEX**: Galaxy Evolution Explorer
**GHz**: Gigahertz ($10^9$ Hz)
**H**: Hydrogen
**HB**: Horizontal Branch
**HCN**: Hydrogen isocyanid
**He**: Helium
**H-R**: Hertzsprung-Russell
**HSC**: Harvard Spectral Classification
**ISM**: Interstellar medium
**ISRF**: Interstellar radiation field
**LTE**: Local thermodynamic equilibrium
**MHz**: Megahertz ($10^6$ Hz)
**MS**: Main sequence
**N**: Nitrogen
**O**: Oxygen
**PHz**: Petahertz ($10^{15}$ Hz)
**PN**: Planetary nebula
**PP**: Proton-proton
**RFI**: Radio frequency interference
**RGB**: Red Giant Branch
**RT**: Radiative transfer
**SE**: Statistical equilibrium
**SGB**: Subgiant Branch

**SRV**: Semiregular variable
**THz**: Terahertz ($10^{12}$ Hz)
**TP-AGB**: Thermal-Pulse Asymptotic Giant Branch
**UV**: Ultraviolet
**ZAMS**: Zero Age Main Sequence

# Chapter 1

# Introduction

Low- and intermediate-mass stars ($0.8$-$8\,M_\odot$) enrich the interstellar medium (ISM) by losing mass and ejecting it into space in the late stages of their life cycle, the asymptotic giant branch (AGB) phase. A cloud of gas and dust surrounding the star, called a circumstellar envelope (CSE), is created. A schematic overview of a CSE is presented in figure 1.1. Through studying these CSEs by looking at observations of molecular species, we can learn a lot about late stellar evolution, CSE chemistry, mass-loss processes and their dependence on stellar properties. However, the CSEs are hard to model precisely.

The photospheric $^{12}$C/$^{13}$C ratio in CSEs is a good tracer of the stellar nucleosynthesis, but it is difficult to make a direct estimate of this ratio from observations. This is because we are unable to distinguish the spectral lines of two isotopes observationally with the currently available observation facilities. The $^{12}$CO/$^{13}$CO isotopologue ratio has therefore been used as a tracer for the $^{12}$C/$^{13}$C ratio (Saberi et al., 2017). However, selective photodissociation by UV radiation is happening to the different CO isotopes in CSEs, where the chemical compounds are broken down by photons, thus impacting the $^{12}$CO/$^{13}$CO isotopologue ratio. The dissociation is selective because it happens through line dissociation (see section 2.3). Furthermore, the $^{12}$CO molecule is more abundant than the $^{13}$CO isotopologue, and is therefore subject to more shielding (see section 2.3.1) than the $^{13}$CO isotopologue (Habing & Olofsson, 2003). This is why the $^{12}$CO/$^{13}$CO abundance ratio is varying when affected by UV radiation. It has also been shown by observations that the $^{12}$CO/$^{13}$CO ratio varies over the CSE (Vlemmings et al., 2013). These facts indicate that the $^{12}$CO/$^{13}$CO ratio can not necessarily be used as a tracer of the $^{12}$C/$^{13}$C ratio, being affected in UV irradiated regions. Instead, it might be preferable to use hydrogen isocyanide (HCN) abundance ratio, H$^{12}$CN/H$^{13}$CN, as this ratio is not affected by UV radiation, making it much more reliable.

In this thesis, we will model CSEs for two different sources, AGB stars W Hydrae and R Leporis, as these stars are close by, UV active, and show a discrepancy with the previously measured $^{12}$C/$^{13}$C and $^{12}$CO/$^{13}$CO abundance ratios. We will look at and perform

radiative transfer analysis of observed $H^{12}CN$ and $H^{13}CN$ lines taken with the Atacama Pathfinder EXperiment (APEX) and the Atacama Large Millimeter/submillimeter Array (ALMA) and compare these with lines created by the model. When good fits between models and data are found, we determine the $H^{12}CN/H^{13}CN$ abundance ratios and compare these to previously measured $^{12}CO/^{13}CO$ and $^{12}C/^{13}C$ abundance ratios, in order to see if they are similar to the C ratios or not. By comparing these ratios, the aim is to quantify the impact of UV radiation on the CO and HCN isotopologue ratios in the outflow of these objects.
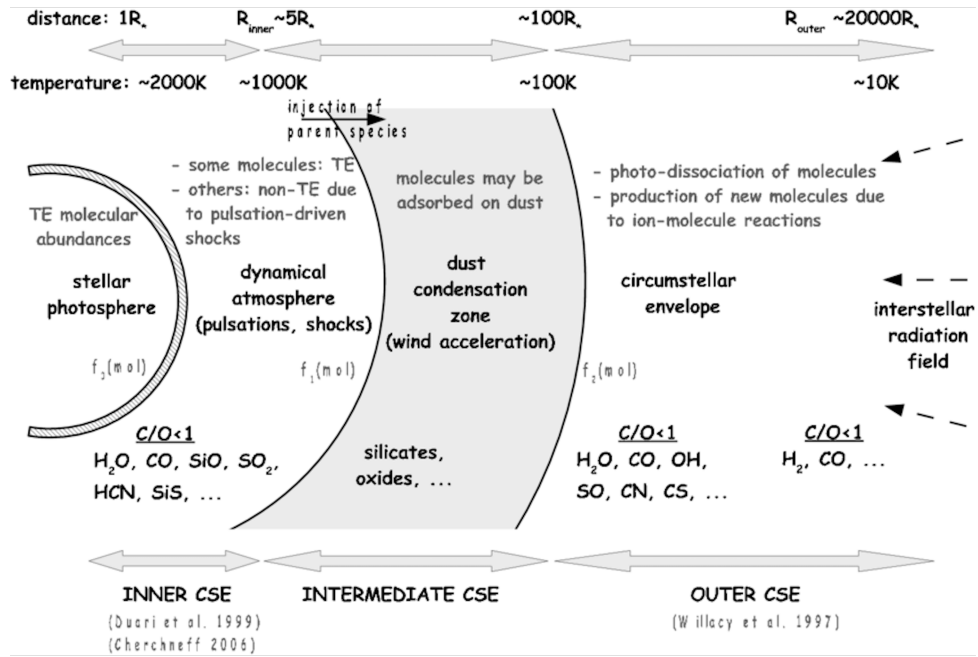


Figure 1.1: Schematic overview of a CSE surrounding an oxygen-rich AGB star. Image is not to scale. Credit: Decin et al. (2010).

# Chapter 2

# Theory

As time goes by, fusion processes happen within the stellar core and the surrounding layers, the stars evolve and move into different stages in their life cycle. The end result of the stellar life depends on different factors, most notably the stellar mass. We will focus mainly on the low- and intermediate-mass stars (0.8-8 $M_{\odot}$), which enter the asymptotic giant branch (AGB) phase in the late stage of their evolution, and the circumstellar envelope (CSE) surrounding them due to the mass loss of the star. These CSEs are complicated as their chemistry and shape can be affected by various aspects such as UV radiation, companion stars and stellar properties, which makes them hard to model but also interesting to investigate further. The CSEs enrich the interstellar medium (ISM), and we want to learn more about their chemistry, mass-loss processes and late stellar evolution. In this section, topics relevant for understanding AGB stars, mass-loss processes and CSEs are presented, in addition to UV radiation and its effect on the CSE chemistry. Additionally, we will look at rotational spectroscopy, a method for investigating the chemical composition in CSEs, and go through basic radiative transfer (RT), a useful technique for interpreting observational data of AGB stars and CSE chemistry.

## 2.1 Stellar evolution

The Hertzsprung-Russell (H-R) diagram is commonly used to categorize stars, presenting stars in different stages in their life cycle. The H-R diagram displays the luminosity and the effective temperature on the y- and x-axis respectively, presented in figure 2.1. The different spectral classes are presented in section 3.2. A star is on the main sequence in the H-R diagram when it fuses hydrogen (H) to helium (He) in the stellar core, so that the core density increases and gravitational potential energy is released. Consequently, half of the energy goes to increasing the gas temperature (thermal energy) and the rest radiates away. A thermal gas pressure sufficiently strong enough to stand against the inward contracting gravitational forces is created, preventing the star from shrinking under the influence of gravity, and maintaining the balance between the forces. A star is in hydrostatic equilibrium when the forces causing the

envelope to contract and expand are in balance (Carroll & Ostlie, 2014). The following theory on stellar evolution is based on *An introduction to modern astrophysics*, second edition, by Bradley W. Carroll and Dale A. Ostlie (Carroll & Ostlie, 2014) and *Mass loss of stars on the asymptotic giant branch* by Höfner and Olofsson (Höfner & Olofsson, 2018).
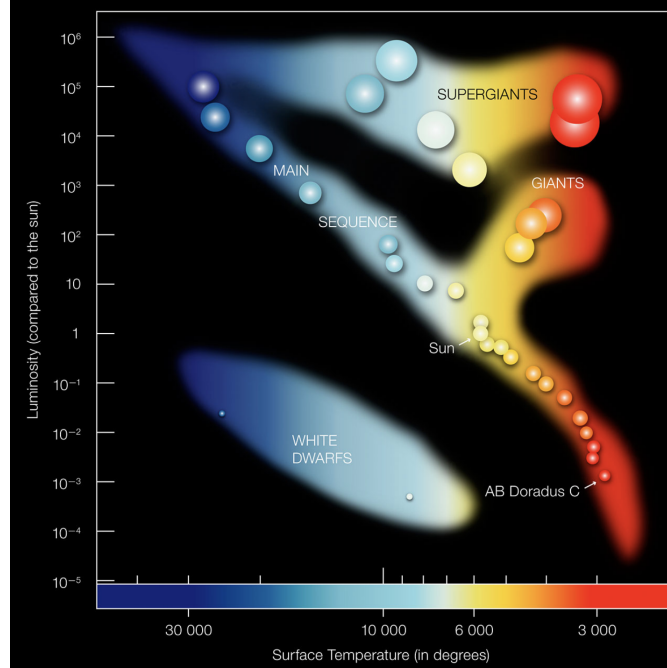


Figure 2.1: Hertzsprung-Russel diagram presenting the stellar life cycle. Image collected from *eso.org* (ESO, 2007).

### 2.1.1 The main sequence

When a star is on the main sequence, H is fused to He through the proton-proton chain (PP-chain) and the carbon-nitrogen-oxygen cycle (CNO-cycle). The PP-chain dominates in stars with masses equal to or less than the Sun and requires a minimum temperature of $4 \times 10^6$ K. This chain can evolve through three different branches, and the first two reactions in all of the chains are:

$$^1_1\text{H} + {}^1_1\text{H} \rightarrow {}^2_1\text{H} + \text{e}^+ + \nu_\text{e}, \tag{2.1}$$

$$^2_1\text{H} + {}^1_1\text{H} \rightarrow {}^3_2\text{H} + \gamma. \tag{2.2}$$
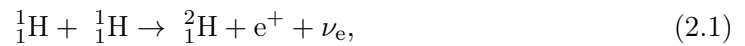
The first reaction is very slow as the decay of a proton to a neutrino on average takes a billion years for an individual proton. Then follows the three branches:

$$\text{ppI} = {}^3_2\text{He} + {}^3_2\text{He} \rightarrow {}^4_2\text{He} + 2\,{}^1_1\text{H} \tag{2.3}$$

$$\text{ppII} \begin{cases} {}^{3}_{2}\text{He} + {}^{4}_{2}\text{He} & \rightarrow & {}^{7}_{4}\text{Be} + \gamma \\ {}^{7}_{4}\text{Be} + \text{e}^{-} & \rightarrow & {}^{7}_{3}\text{Li} + \nu_{\text{e}} \\ {}^{7}_{3}\text{Li} + {}^{1}_{1}\text{H} & \rightarrow & 2\,{}^{4}_{2}\text{He} \end{cases} \tag{2.4}$$

$$\text{ppIII} \begin{cases} {}^{3}_{2}\text{He} + {}^{4}_{2}\text{He} & \rightarrow & {}^{7}_{4}\text{Be} + \gamma \\ {}^{7}_{4}\text{Be} + {}^{1}_{1}\text{H} & \rightarrow & {}^{8}_{5}\text{B} + \gamma \\ {}^{8}_{5}\text{B} & \rightarrow & {}^{8}_{4}\text{Be} + \text{e}^{+} + \nu_{\text{e}} \\ {}^{8}_{4}\text{Be} & \rightarrow & 2\,{}^{4}_{2}\text{He} \end{cases} \tag{2.5}$$
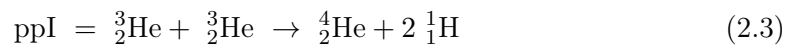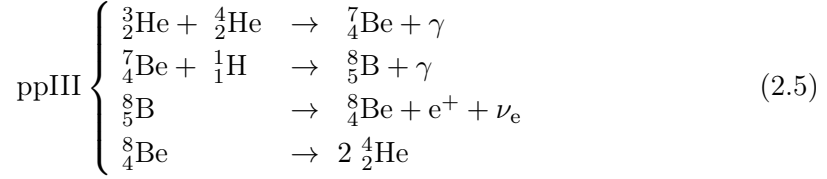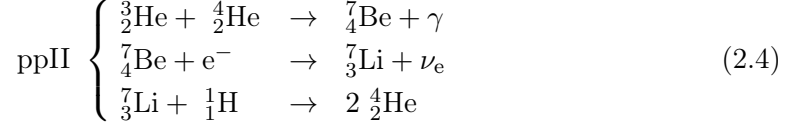
where $\nu_{\text{e}}$ is the electron neutrino produced, and the $\gamma$s are energy outputs from each reaction (Salaris & Cassisi, 2005).

The CNO-cycle is dominant in stars with masses larger than $1.3\,\text{M}_{\odot}$ (Salaris & Cassisi, 2005), as it is much more temperature dependent than the PP-chain, and is effective at temperatures above $10^{7}\,\text{K}$. The two first branches in the CNO cycle are presented below,

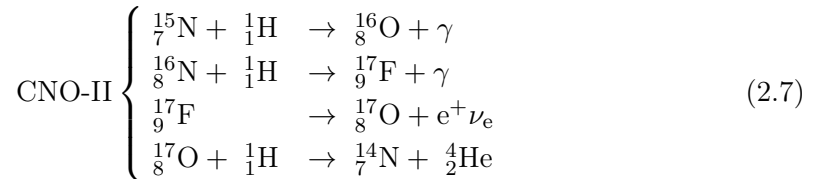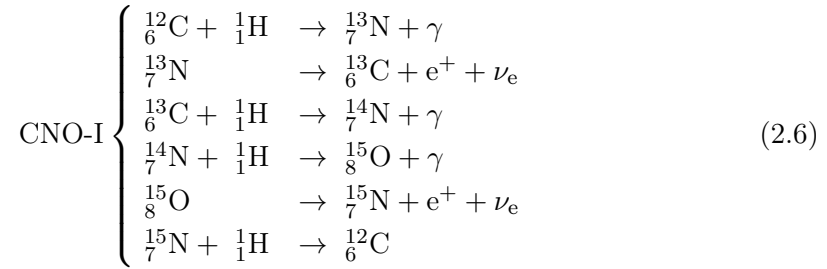$$\text{CNO-I} \begin{cases} {}^{12}_{6}\text{C} + {}^{1}_{1}\text{H} & \rightarrow & {}^{13}_{7}\text{N} + \gamma \\ {}^{13}_{7}\text{N} & \rightarrow & {}^{13}_{6}\text{C} + \text{e}^{+} + \nu_{\text{e}} \\ {}^{13}_{6}\text{C} + {}^{1}_{1}\text{H} & \rightarrow & {}^{14}_{7}\text{N} + \gamma \\ {}^{14}_{7}\text{N} + {}^{1}_{1}\text{H} & \rightarrow & {}^{15}_{8}\text{O} + \gamma \\ {}^{15}_{8}\text{O} & \rightarrow & {}^{15}_{7}\text{N} + \text{e}^{+} + \nu_{\text{e}} \\ {}^{15}_{7}\text{N} + {}^{1}_{1}\text{H} & \rightarrow & {}^{12}_{6}\text{C} \end{cases} \tag{2.6}$$

$$\text{CNO-II} \begin{cases} {}^{15}_{7}\text{N} + {}^{1}_{1}\text{H} & \rightarrow & {}^{16}_{8}\text{O} + \gamma \\ {}^{16}_{8}\text{N} + {}^{1}_{1}\text{H} & \rightarrow & {}^{17}_{9}\text{F} + \gamma \\ {}^{17}_{9}\text{F} & \rightarrow & {}^{17}_{8}\text{O} + \text{e}^{+}\nu_{\text{e}} \\ {}^{17}_{8}\text{O} + {}^{1}_{1}\text{H} & \rightarrow & {}^{14}_{7}\text{N} + {}^{4}_{2}\text{He} \end{cases} \tag{2.7}$$

When all the H in the core has burnt up, a core consisting of He remains. The thermal gas pressure is now no longer strong enough to stand against the inward contracting gravitational forces, which becomes dominant and the core starts to contract. The balance between the forces is no longer maintained, consequently the star is no longer in hydrostatic equilibrium and starts to move off the main sequence.

As the core contracts, gravitational potential energy is released. Consequently a thick shell of H starts to burn as the temperature outside the core increases sufficiently. The core radius then decreases and the luminosity increases slightly. The shell continues

to burn H, thus the core increases in mass until it reaches the Schönberg-Chandrasekhar limit, which is defined as "the maximum fraction of a star's mass that can exist in an isothermal core and still support the overlying layers" (Carroll & Ostlie (2014), p. 497). The core then starts to contract rapidly, leading to expansion of the overlying envelope and a decrease in temperature. This is called the subgiant branch (SGB) Carroll & Ostlie (2014). In figure 2.2, a schematic H-R diagram of the different stages of evolution for a $5\,M_\odot$ star is presented, from Zero Age Main Sequence (ZAMS) to white dwarf phase, where ZAMS is the time when a star first enters the main sequence. The different stages of stellar evolution labeled in the figure will explained in the following sections.
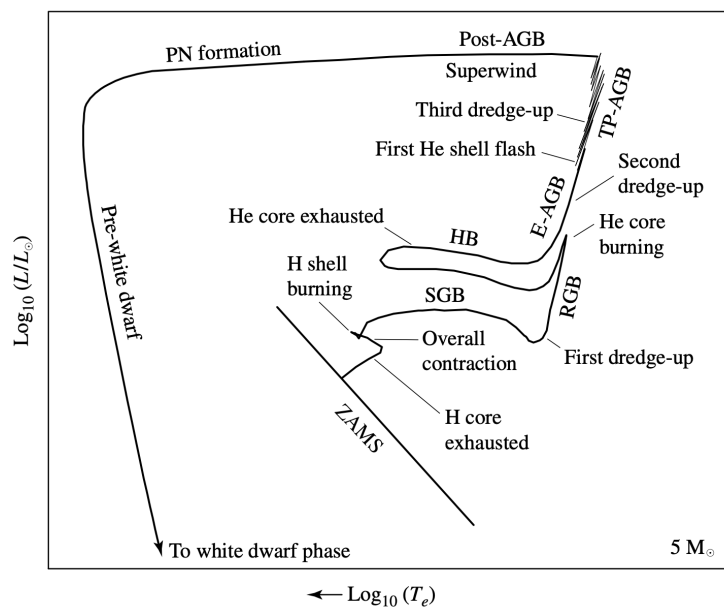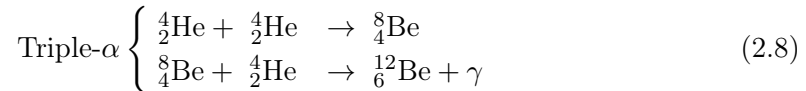


Figure 2.2: A schematic H-R diagram presenting the evolution of a $5\,M_\odot$ star from Zero Age Main Sequence (ZAMS) to white dwarf phase. Credit: Carroll & Ostlie (2014).

### 2.1.2   Red giant branch stars

As the stellar envelope expands and the effective temperature decreases, the star becomes larger, cooler and redder. It has entered the red giant branch (RGB) and is now a red giant (see figure 2.2). Fusion of He in the core of the red giant produces a stellar core consisting of carbon (C) and oxygen (O), a C-O core. A convection zone near the surface is created as the stellar envelope expands and the temperature decreases. As the evolution of the star continues, the base of this convection zone will extend deep into the star's interior, transporting material chemically modified by nuclear processes from deep regions of the star to the surface, mixing the processed material with the material above. This transport of materials is known as the first dredge-up phase (Carroll & Ostlie, 2014). These dredge-ups are essential for collecting information about stellar

nucleosynthesis from observations.

At the tip of the RGB, the central temperature and density are now high enough to start fusion of He to C through the triple-alpha process,

$$
\text{Triple-}\alpha \begin{cases} {}^{4}_{2}\text{He} + {}^{4}_{2}\text{He} & \rightarrow {}^{8}_{4}\text{Be} \\ {}^{8}_{4}\text{Be} + {}^{4}_{2}\text{He} & \rightarrow {}^{12}_{6}\text{Be} + \gamma \end{cases} \tag{2.8}
$$

The H burning shell remains the dominant source of the star's luminosity, thus as the core expands, the shell is pushed outwards, resulting in a decrease in luminosity at the same time as the effective temperature starts to increase again. This phase is called the red giant tip (Carroll & Ostlie, 2014). Directly after the red giant tip follows the horizontal branch (HB), where the triple-alpha process fuses He in the core and the CNO cycle fuses H in the surrounding shell (see figure 2.2). When the star reaches its most blueward point, the core starts to contract due to the increased mean molecular weight of the core, which thus increases the core temperature. Consequently, the He-burning shell gets stronger and the material above expands and cools, which temporarily turns off the H-burning shell. After a while, as the core continues to contract, it will cool due to the increase in neutrino production (Carroll & Ostlie, 2014). After the low- and intermediate-mass stars come out of the subsequent central He-burning stage, leaving a C-O core, the nuclear burning in the stellar core is over for these stars and they enter the AGB phase.

### 2.1.3   Asymptotic giant branch stars

The AGB phase is a late stage in the evolution of a low- and intermediate-mass star ($0.8$-$8 \, \text{M}_\odot$). AGB stars are cool, luminous stars placed above the RGB stars on the H-R diagram (see figure 2.2). They have lower effective temperatures, in the range of 1500-3000 K (Carroll & Ostlie, 2014), high luminosities, a few $10^3$ to a few $10^4 \, \text{L}\odot$, and typically a radius of several hundred solar radii. They are powered by the burning of H and He in thin layers surrounding the C-O core. This stage is the final evolutionary stage before the star becomes a white dwarf (Höfner & Olofsson, 2018).

In the early-AGB phase (E-AGB) the star consists of a core of C-O followed by a He-burning shell, a He shell, and then a H-burning shell surrounded by a H,He envelope (see figure 2.3). At this stage, the H-burning shell is nearly inactive and the He-burning shell is the dominant source of output energy. Then a second dredge-up happens, this time leaving a convection zone reaching even deeper into the star's interior.
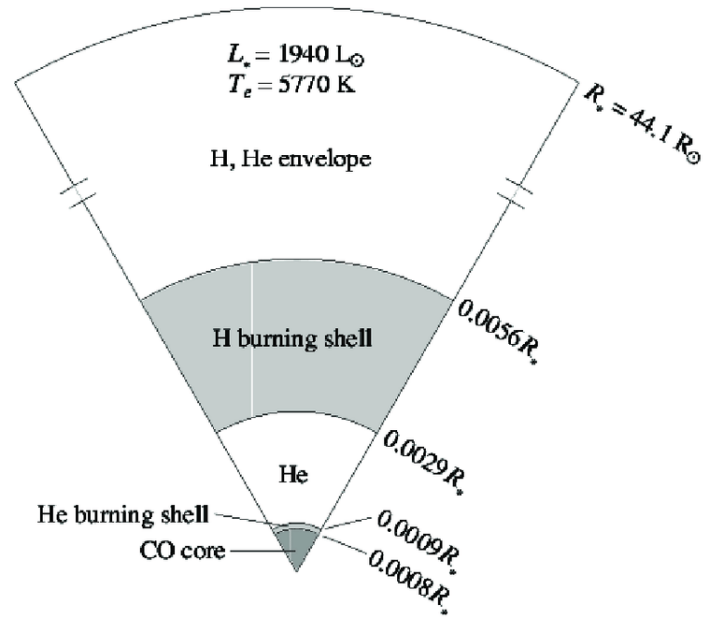
Figure 2.3: Schematic illustration of the structure of a $5\,M_\odot$ AGB star. Image is not to scale. Credit: Carroll & Ostlie (2014).

### 2.1.4   Thermal-pulse AGB and helium shell flashes

Near the upper portion of the AGB phase (see figure 2.2), called the thermal pulse AGB (TP-AGB), the H-burning shell will eventually awaken and again become the star's dominant source of energy output, as the decreasing He-burning shell will start to turn on and off quasi-periodically and create what is called helium shell flashes. These occur because He ash is dumped from the H-burning shell onto the underlying He layer. Consequently, the base of the He shell becomes slightly degenerate as the mass of the shell increases. The He shell base temperature increases sufficiently so that a helium flash occurs, pushing the H-burning shell outwards, thus cooling it down and turning it off for some time. Eventually, the process will be repeated as the H-burning shell recovers and the burning in the He shell decreases. For stars near $5\,M_\odot$, the period between these pulses can be thousands of years, and hundreds of thousands of years for lower mass stars around $0.6\,M_\odot$ - the period time is a function of star mass (Carroll & Ostlie, 2014).

As a consequence of the increase in energy flux during a helium shell flash, a third dredge-up happens. Now the convection zone reaches even deeper into the star's interior, bringing up C-rich material to the surface, affecting the star's ratio of O to C. Multiple third dredge-ups can happen, consequently transforming an O-rich spectrum to a C-rich spectrum over time. The three chemical types of AGB stars are C-rich (C/O > 1), S-type (C/O ≈ 1) and O-rich (M-type C/O < 1). As previously mentioned, the dredge-ups are important for collecting information about stellar nucleosynthesis from

observations. In our thesis, we look at observations of an O-rich and a C-rich AGB star (see section 3.3) and compare our results with previously measured CO and C ratios (see section 6.1). The dredge-ups make it possible to collect necessary information about elements relevant to our research question (see section 1).

### 2.1.5 Mass loss

After the TP-AGB phase, in stars with original masses of $8\,M_\odot$ or less, more and more of the He in the He-burning shell will first be converted into C and then into O, thus increasing the mass of the C-O core as it at the same time contracts slowly. This will increase the central density in the core sufficiently enough so that electron degeneracy pressure begins to dominate.

Nuclear burning in the C-O core of stars with ZAMS masses less than $4\,M_\odot$ will never happen because the core will never become large or hot enough. But, according to theory, if the effects of mass-loss are ignored, when the C-O core mass increases sufficiently for AGB stars with initial masses between 4-8 $M_\odot$, the hydrostatic equilibrium in the core can no longer be maintained, even with the help from the degenerate electron gas pressure. A catastrophic core collapse should then happen, but it does not. The reason for this is the enormous mass-loss rates, causing the core mass to never exceed the Chandrasekhar limit - "the maximum value of $1.4\,M_\odot$ for a completely degenerate core" (Carroll & Ostlie (2014), p. 514). Compositions of O, neon, and magnesium are created in the core due to additional nucleosynthesis in stead of collapse.

In order for mass loss to happen, the atmospheric gas needs to be accelerated beyond the escape velocity, and for such an event to happen, a process sufficiently effective enough is required, e.g. shock waves triggered by stellar pulsation. It is also believed that the mass-loss mechanisms has something to do with the helium shell flashes (Carroll & Ostlie, 2014). The AGB star's high luminosity and low surface gravity, $\approx$ 4-5 orders of magnitude lower than for a Sun-like star, which in combination with radiation pressure on the dust grains makes it easier for the material to escape from the surface layers, may also be a possible cause of mass loss. Our understanding of the mass-loss mechanisms is currently poor.

Nevertheless, as the star loses mass, escaping materials of gas and dust are ejected into space creating a surrounding cloud called a circumstellar envelope (CSE). As the evolution of the AGB star continues, the mass decreases as the luminosity and radius increase, leading to an acceleration in mass-loss rate with time, which also indicates an even lower surface gravity and thus surface material that is less tightly bound. In addition, a so called superwind is developed in the very end of the AGB evolution, resulting in a huge mass-loss rate of $10^{-4}\,M\odot/yr$. After a long period of increasing mass loss during the AGB evolution, this is the final mass-loss stage.

As mentioned, our current understanding of the mass-loss mechanisms is poor. In

order to be able to develop a good theory of mass loss of AGB stars, a realistic model of wind acceleration, which is hard to understand, is needed. At the present time, it is not possible to precisely predict the mass-loss rate of AGB stars based only on stellar parameters. A better understanding of the mass-loss process can be achieved by studying various properties of the CSE, such as magnitude, geometry and composition, and its dependence on stellar parameters, e.g. mass, metallicity and luminosity. Information about the chemical composition and sizes of dust grains can be obtained by high-angular resolution observations (Höfner & Olofsson, 2018).

### 2.1.6 Post-AGB and planetary nebulae

As the star enters the post-AGB phase (see figure 2.2), where it continues to lose mass, the expanding cloud eventually becomes optically thin and exposes the hot central star. The star will then cool down and become a white dwarf, which is basically the old degenerate C-O core of the red giant surrounded by a thin layer of H and He remains ejected from the star. As time goes by, the CSE will evolve into a planetary nebula (PN), surrounding the white dwarf progenitor.

## 2.2 Circumstellar envelopes

As an AGB star loses mass, it ejects massive outflows of gas and dust into space, consequently enriching the ISM with materials originating from deep within the star brought to the surface by the convection zones during the dregde-up phases. This escaping material creates a CSE, a cloud of gas and dust, surrounding the AGB star. An illustration of an AGB star and its CSE is presented in figure 2.4, and an image taken with the Atacama Large Millimeter/submillimeter Array radio telescope (ALMA) showing a CSE surrounding the star R Sculptoris is presented in figure 2.5.
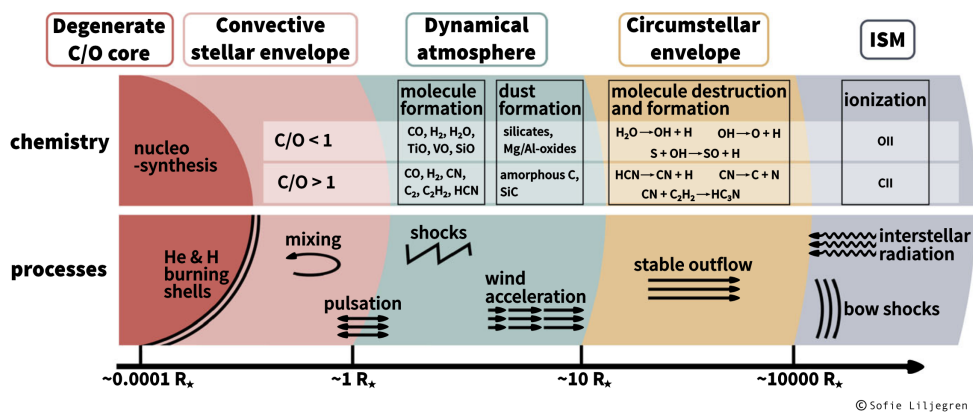


Figure 2.4: An illustration showing the physical processes in an AGB star and its CSE. Image collected from Höfner & Olofsson (2018). Credit: S. Liljegren.
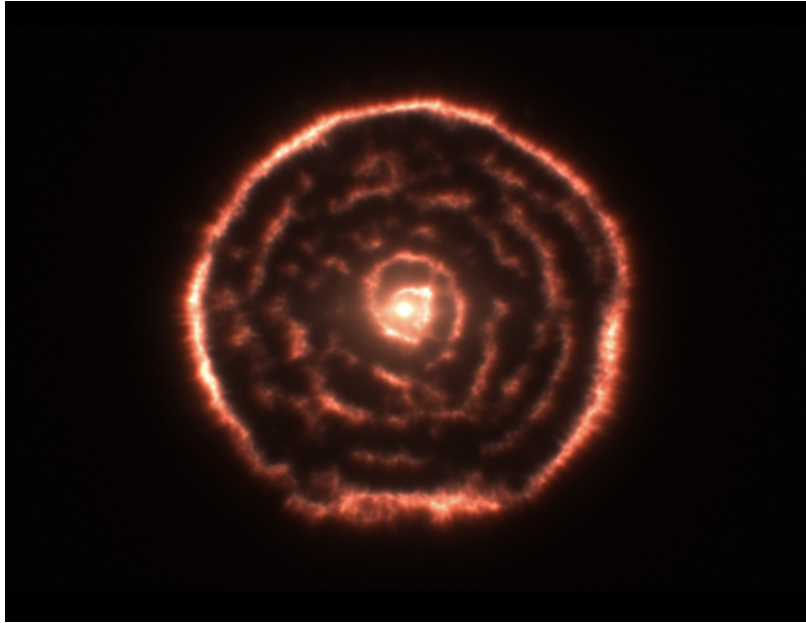
Figure 2.5: Observations of $^{12}$CO transition 3-2 taken with the Atacama Large Millimeter/submillimeter Array (ALMA) in the submillimetric wavelengths of AGB star R Sculptoris showing the CSE surrounding it. This particular CSE has the shape of a spiral, which most likely is due to the presence of a companion star. Image collected from ESO (2012).

### 2.2.1  Mass-loss rate dependence on stellar properties

The mass-loss rate depends on stellar properties like mass, luminosity, effective temperature, and metallicity. In order to better understand CSEs, we need to look at the mass-loss rates. In 1975, Reimers, D. (1975) introduced a relation describing the dependence of mass-loss rate on stellar characteristics, based on observations of cool, giant stars, to be:

$$\dot{M} \propto L_* R_* / M_*, \tag{2.9}$$

where $\dot{M}$ is the mass-loss rate and $L_*, R_*$ and $M_*$ are the star's luminosity, radius and mass respectively. This attempt on determining the empirical mass-loss law with a simple relation was later shown to not be a satisfactory description of AGB mass loss (Höfner & Olofsson, 2018). The relation is more complicated as different factors may affect the mass-loss rate.

**Effective temperature**

It is expected that the temperature in the stellar atmosphere affects dust condensation and thus mass loss. Höfner & Olofsson (2018) summarize that no obvious mass-loss rate

dependency on the effective temperature is found for low- and intermediate mass-loss rate stars, but that when higher mass-loss rate stars are included, a small increase in mass-loss rate as the effective temperature decreases is seen for C stars.

### Metallicity

Metallicity is defined as the abundance of elements that are heavier than H and He with respect to H. Cummings et al. (2016) came to the conclusion that the total amount of the mass loss did not strongly depend on the metallicity, but that the terminal wind velocity and dust-mass-loss rate decreases with metallicity. This is the case mostly for O-rich stars, and, if the metallicity is sufficiently low, also for C-rich stars (Höfner & Olofsson, 2018).

### Luminosity

The mass-loss rate shows a positive luminosity dependence, but an exact scaling law is difficult to identify, due to the large scatter in data. Also, the luminosity often changes together with other parameters, e.g. mass and effective temperature, during the AGB evolution. So when separating the luminosity dependence, the main problem is caused by the influence of these parameters (Höfner & Olofsson, 2018). A study of nearby AGB stars by Danilovich et al. (2015) presents a scaling law

$$\dot{M} \propto L_*^5, \tag{2.10}$$

which is not unreasonable, as this means that the range of mass-loss rates can be connected to a range in luminosity corresponding to a factor of around 4 (Höfner & Olofsson, 2018). Other scaling laws found through different studies have also been presented, mainly for extragalactic objects (e.g. Goldman et al. (2017), Jiménez-Esteban & Engels (2015), Srinivasan et al. (2009) and Groenewegen et al. (2009)). Nevertheless, no profitable scaling law has been formulated.

### Pulsation properties

Another property that may have an impact on the mass-loss rates is the pulsation properties, the regularity and amplitude of the pulsation. Höfner & Olofsson (2018) summarize that based on observations of the three chemical types of AGB stars, C-rich, S-type, and O-rich, an obvious positive trend of mass-loss rate with period is found in the range of 300 to 800 days, and that stars with periods longer than 800 days has reached their maximum mass-loss rate. Additionally, the mass-loss rates for Mira and semiregular variables (SRV), stars whose brightness fluctuates when seen from Earth, in the period range 300 to 400 days appear to cover basically the same mass-loss range as for SRVs with periods of less than 200 days. To summarize, the mass-loss rates increase with pulsation period, but has a saturation effect when the period is longer than 800 days (Höfner & Olofsson, 2018).

**Mass**

It is difficult to determine the effects stellar mass has on mass-loss rate, as the observed sources have different masses, both initial and current, even though it is probable that the current mass of the AGB stars affects the mass loss as it defines the gravitational potential. It is difficult to determine, but it should be possible, if other parameters are pinned down, to find it by use of the pulsation properties of the star (Höfner & Olofsson, 2018). In 2007, Wood (2007) found no obvious connection between the mass-loss rate and current star mass.

### 2.2.2 Effects on CSEs from companion stars

A companion star can affect both the AGB star and the large-scale structure of the CSE, by shaping the wind of the star with its gravity and radiation, and, depending on the distance, it may also affect the physics of the mass-loss process. Consequently, the companion star can enhance the outflow by modifying the gravitational potential of the AGB star and adding angular momentum to the outer layers. The two main effects a companion star has on the CSE are that it directs CSE material to the orbital plane, which consequently flattens the CSE, and that the density structure of the CSE is modulated, which then can take the form of a spiral (in 3D). The first is caused by the gravitational attraction of the companion, and the second is a consequence of the reflex motion of the mass-losing star (Höfner & Olofsson, 2018).

Other characteristics of the companion star, like a strong wind, can also alter the conditions of the wind acceleration region of the AGB star. In addition, if the companion star has a hot radiation field, this might affect the dust formation negatively (Höfner & Olofsson, 2018). Another non-gravitational effect the companion star can have on the CSE is UV radiation, which will be explained further in section 2.3.1. Determining the shape of a CSE from observations is a complicated process. In the case of exposure to UV radiation, the RT modelling of dust and line emission using the standard CSE model, where sphericity is assumed, is unreliable for deriving the mass-loss rate, because the distortion of the CSE is so large.

## 2.3 UV radiation

Ultraviolet (UV) radiation is electromagnetic radiation in the wavelength range from 10 nm to 400 nm (30 PHz to 750 THz). Molecular photodissociation/photoionization by UV radiation affects the chemistry of the CSE surrounding the AGB star. Whether the dissociation happens through line dissociation (molecular dissociation only from absorption at specific frequencies) or continuum dissociation (molecular dissociation from all absorptions) depends on the structure of the molecule (Saberi et al., 2019). As mentioned in section 1, the dissociation of CO happens through line dissociation, as opposed to the dissociation of hydrogen isocyanide (HCN), the molecule we observe, which happens through continuum dissociation. Molecules with line dissociations are subject

to selective photodissociation. Consequently, exposure to UV radiation can cause variations of their isotopologue ratios from the initial abundance (where isotopologues are molecules that have a different isotopic composition than their parent molecule). This is due to the different amounts of shielding, which depend on the molecular abundances.

### 2.3.1 Influence of UV radiation on CSE chemistry

By studying molecules and isotopic ratios in CSEs, we can obtain information about several different factors, such as the AGB stars' impact on the ISM and their chemical enrichment, their initial mass and stage in evolution. CO is the most abundant species in the CSEs, next to $H_2$, and is therefore amongst other things a great mass-loss rate estimator, by looking at CO rotational line emission at millimeter/submillimeter wavelenghts. The energy levels are easily collisionally exited, and this factor combined with the high abundance gives us strong lines. Additionally, the energy level structure is simple (Höfner & Olofsson, 2018).

The photospheric $^{12}C/^{13}C$ ratio is a good tracer of the stellar nucleosynthesis. The deep convection zones created during the stellar evolution (see section 2.1.2) transport material chemically modified by nuclear processes to the surface from regions deep into the star's interior. During the third dredge-up phase (see section 2.1.4), C-rich materials are brought to the surface, but it is difficult to make a direct estimate of the $^{12}C/^{13}C$ ratio from observations (Saberi et al., 2017). This is because the spectral lines of two isotopes can not be distinguished observationally with the currently available observation facilities. The $^{12}CO/^{13}CO$ ratio has been used as a tracer of the photospheric $^{12}C/^{13}C$ ratio, however CO is affected by UV radiation, as mentioned in section 2.3, by dissociation through line dissociation.

Photodissociation is the dominant process destroying CO and determining the abundance distribution of CO at the outer CSE. It happens at wavelength range 911.75-1117.8 Angstrom (Saberi et al., 2019). The reason the $^{12}CO/^{13}CO$ abundance ratio is varying is because the $^{12}CO$ molecule is more abundant than the $^{13}CO$ isotopologue, thus it is subject to more shielding than the $^{13}CO$ isotopologue. This shielding includes self-shielding and mutual shielding. Self-shielding is the process where the CO molecule closer to the UV source absorbs the UV photons with a specific wavelength that may result in its dissociation, and mutual shielding is shielding by other abundant species, e.g. $H_2$ and dust particles which are dissociated at the same wavelengths (Saberi et al., 2019). When UV photons are absorbed by dust in the CSE, it causes the dust to slightly increase in temperature. As a consequence, the dust reradiates, as a blackbody, the absorbed energy in the far-infrared/mm part of the spectrum. Thus the $^{12}CO/^{13}CO$ ratio will vary as $^{12}CO$ and $^{13}CO$ are affected differently by the UV radiation.

High resolution ALMA observations have also shown that the $^{12}CO/^{13}CO$ ratio varies over the CSE, indicating that this ratio not necessarily can be used as a reliable tracer for the photosperic value, as it is affected in UV irradiated regions (Saberi et al.,

2017). Instead, it is suggested to use the isotopologue $H^{12}CN/H^{13}CN$ ratio. This ratio is not affected by UV radiation as the $H^{12}CN$ and $H^{13}CN$ molecules are equally affected by UV radiation, as dissociation happens through continuum dissociation (see section 2.3). It is important to have a correct estimate of the tracer of C as this can tell us a lot about the stellar nucleosynthesis. It is therefore of interest in this thesis to investigate to whether the $H^{12}CN/H^{13}CN$ abundance ratios in CSEs can be a better tracer of the $^{12}C/^{13}C$ ratio, by comparing our results with previously measured $^{12}CO/^{13}CO$ and $^{12}C/^{13}C$ ratios.

### 2.3.2 Sources of radiation

The source of the radiation can be external, e.g. the interstellar radiation field (ISRF), or internal, e.g. the AGB star itself and the stellar activity in the chromosphere or a close companion star. O- and B-type stars, which are large, luminous and heavy stars (see section 3.2), are the main sources of UV radiation from the ISRF. How much the CSE chemistry is affected depends on the strength of the field, and how much the ISRF manages to penetrate into the CSE depends on parameters like clumpyness, geometry and the composition of dust in the cloud. The UV radiation will penetrate deeper into the CSE if the clumpyness is high in comparison to a less clumpy CSE with the same average column density (Meixner et al., 1992), and as a consequence the chemical composition in the CSE can be changed (Van de Sande et al., 2018).

## 2.4 Rotational spectroscopy

It is possible to investigate the chemical composition of CSEs by looking at molecules in the gas phase and the energies between their quantized rotational states ($J$). This method of measuring the rotational transitions is called rotational spectroscopy. The rotational transitions have energies proportional to 1-10 cm$^{-1}$, meaning they lie at 0.1-10 mm. Rotational spectroscopy is referred to as microwave spectroscopy (McQuarrie, D. A., 2007). The following expression describes the energy difference between rotational level $J$ and $J+1$:

$$E_{J+1} - E_J = B(J+1)(J+2) - BJ(J=1) = 2B(J+1), \qquad (2.11)$$

where $J$=0,1,2,.., the photon energy is $E = h\nu$ ($h$ is the Plack constant and $\nu$ is the photon frequency) and $B = \hbar^2/2I$ is the rotational constant ($\hbar$ is $1.05457\times10^{-34}$ m$^2$kg/s and $I = \mu l^2$ is the moment of inertia) (McQuarrie, D. A., 2007). The rotational energy levels $J$ are illustrated in figure 2.6. It is common to use the unit cm$^{-1}$ (wave numbers) in spectroscopy, so in order to convert from units of energy to the unit of wave number, $B$ is written as

$$B = \tilde{B} = \frac{h}{8\pi cI}, \qquad (2.12)$$

where $c = 2.998 \times 10^{10}$ cm/s is the speed of light.

Molecular excitation can occur by collision or radiation. A molecule can get excited to a higher energy level $J$ by colliding with a particle which transfers enough kinetic energy to excite the molecule. Another possibility is when a molecule is hit by a photon and absorbs the radiation. The energy needed for the transition to happen has to be equal to the energy of the photon. In the inner region of the CSE, the $H_2$ gas density is higher, thus the collision rate is greater. In addition, the radiation from the central star is stronger. Consequently, molecules get excited more easily in the inner regions than in the outer, as a higher gas density increases the probability of many molecules getting excited to higher energy levels by collision. The higher $J$ transition, the more energy is needed for a transition to happen (see figure 2.6). We therefore expect the higher $J$ transitions, e.g. 10 to 9, to probe the inner region of the CSE, as this is where it is most likely to find molecules in higher energy states. In the outer parts of the CSE, the gas density and temperature are lower. Therefore, we expect low $J$ transitions which require less energy, e.g. 2 to 1, to get excited at the outer regions.

In this thesis, we will look at the rotational line observations of HCN in CSEs, both $H^{12}CN$ and $H^{13}CN$, in order to calculate the abundance ratio between them. HCN is a linear molecule, with a triple bond between C and nitrogen (N) and can be observed by looking at the transitions between rotational energy levels. As explained in section 2.3.1, we are interested in learning more about the $H^{12}CN/H^{13}CN$ abundance ratio in CSEs as this might be a more reliable tracer for the $^{12}C/^{13}C$ ratio than the $^{12}CO/^{13}CO$ ratio, which is affected by UV radiation. We will later compare this $H^{12}CN/H^{13}CN$ ratio with previously measured $^{12}CO/^{13}CO$ and $^{12}C/^{13}C$ ratios to gain knowledge about the impact of UV chemistry in the CSEs.
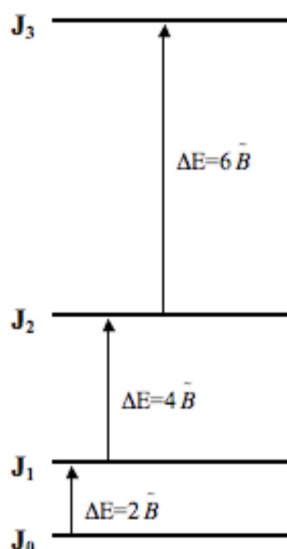


Figure 2.6: Rotational energy levels (McQuarrie, D. A., 2007).

## 2.5   Radiative transfer

Radiative transfer (RT) describes how radiation propagates through a medium, and how the radiation is affected by absorption, emission, and scattering processes. It is described mathematically through the RT equation,

$$\frac{dI_\nu}{ds} = -\kappa_\nu I_\nu + \epsilon_\nu, \tag{2.13}$$

where $I_\nu$ is the intensity along the line of sight in unit $\mathrm{erg}/(\mathrm{cm}^2\,\mathrm{s\,sr\,Hz})$ $\kappa_\nu$ is the linear absorption coefficient in unit $\mathrm{cm}^{-1}$ and $\epsilon_\nu$ is the emissivity in unit $\mathrm{erg}/(\mathrm{cm}^3\,\mathrm{s\,sr\,Hz})$, all at frequency $\nu$ (Hz). The first term is the "loss term" describing how much intensity is lost from the beam, and the second term describes how much intensity is added to the beam, after passing a distance $s$. If there is only emission or only absorption, $\kappa_\nu = 0$ or $\epsilon_\nu = 0$ respectively (Wilson et al., 2013). Equation (2.13) can be rewritten in order to express the change in intensity by use of the optical depth. The ratio between $\epsilon_\nu$ and $\kappa_\nu$, called the source function $S_\nu$, and the optical depth, $\tau_\nu$, can be defined as

$$\frac{\epsilon_\nu}{\kappa_\nu} \equiv S_\nu, \tag{2.14}$$

and

$$d\tau_\nu = -\kappa_\nu ds. \tag{2.15}$$

By inserting equation (2.14) and (2.15) into (2.13), the RT equation can be written as

$$\frac{dI_\nu}{d\tau_\nu} = I_\nu - S_\nu, \tag{2.16}$$

which is a first order differential equation with the following solution,

$$I_\nu(\tau_\nu) = I_\nu(0)\, e^{-\tau_\nu} + \int_0^{\tau_\nu} S_\nu(t_\nu)\, e^{-(\tau_\nu - t_\nu)} dt_\nu, \tag{2.17}$$

where $I_\nu(0)$ is the background intensity and $t_\nu$ is the optical depth we integrate over. The first term describes how much radiation is absorbed from the background intensity and the second term describes how much radiation is emitted and re-absorbed.

The source function (equation 2.14) can also be expressed by use of Einstein coefficients when describing a transition between two states, $u$ and $l$,

$$S_{ul} = \frac{n_u A_{ul}}{n_l B_{lu} - n_u B_{ul}}, \tag{2.18}$$

where $A_{ul}$ is the Einstein coefficient for spontaneous de-excitation and $B_{lu}$ is the Einstein coefficient for radiative excitation, from state $u$ to state $l$ and $l$ to $u$ respectively, and

$n_u$ and $n_l$ are the populations of level $u$ and $l$. In statistical equilibrium (SE), which is what we consider when calculating the molecular level populations, the radiation fields in all directions and frequencies, as well as the molecular level populations, do not vary in time, indicating that the rate equation is

$$\frac{\mathrm{d}n_i}{\mathrm{d}t} = 0. \tag{2.19}$$

Following, the SE system of equations can be given as

$$\sum_{l<u}[n_u A_{ul} - (n_l B_{lu} - n_u B_{ul})\overline{J}_{ul}]-$$
$$\sum_{l>u}[n_l A_{lu} - (n_u B_{ul} - n_l B_{lu})\overline{J}_{ul}]+$$
$$\sum_{u,l}(n_u C_{ul} - n_l C_{lu}) = 0, \tag{2.20}$$

where $C_{ij}$ is the Einstein coefficient for collisional excitation and de-excitation ($C_{lu}$ is the number of collisional excitations from state $l$ to $u$ and $C_{ul}$ is the number of collisional de-excitations from state $u$ to $l$, both per second per particle in the first index state), and $\overline{J}$ can be expressed as

$$\overline{J} = \frac{1}{4\pi} \int d\Omega \int d\nu \theta_\nu(\mu) I_\nu(\mu), \tag{2.21}$$

which is the mean intensity we get when we integrate the specific intensity $I_\nu$ over $\Omega$ (solid angle) and averaged over all directions $\mu$. $\theta_\nu$ is a weight function and $I_\nu$ is the specific intensity with frequency $\nu$ along direction $\mu$. The radiative transfer equations are presented in more detail in Rutten, R. J. (2003) and Rybicki, G. B. and Hummer, D.G (1991). The code that will be used to interpret observational data in this thesis solves equation 2.17 and 2.20. This code will be presented in Chapter 4.

# Chapter 3

# Sources and data

When trying to find how much the UV chemistry affects the CSEs chemistry, we select two UV bright AGB stars observed with GALEX (Galaxy Evolution Explorer) (NASA JPL, Accessed: 2022-04-26). We then compare $^{12}CO/^{13}CO$ and $^{12}C/^{13}C$ ratios from previous research with the $H^{12}CN/H^{13}CN$ abundance ratios we find. In this section, we will go through some basic radio astronomy and look at the two radio telescopes used to obtain the data, ALMA (Atacama Large Millimeter/submillimeter Array) and APEX (Atacama Pathfinder EXperiment). A general description of the different spectral classes will be given, as well as a presentation of the two sources from which we have received observational data. Frequencies, energies and $J$ transitions for each molecule observed are also presented.

## 3.1 Radio astronomy

Some information from stars, e.g. information about the photosphere, can be obtained by looking in the optical wavelength range, since they are radiating as a consequence of their high temperatures. Nevertheless, a lot of information is not visible to the naked eye and other techniques are therefore required, e.g. radio astronomy techniques. These techniques are beneficial and necessary when observing emission lines from evolved stars as looking at the millimeter and submillimeter part of the spectrum can reveal characteristics that are otherwise hidden in visible light. In addition, looking at this part of the spectrum allow us to observe molecular line transitions for $H^{12}CN$ and $H^{13}CN$ (see section 2.4). Another favorable trait of using radio telescopes is that they can be used both day and night, the radiation is still detectable as the light from the Sun does not affect the observations and the atmosphere is transparent to radio waves. In addition to the following description of radio astronomy, see Wilson et al. (2013) and Wilson (2018) for more information.

### 3.1.1   The radio window

Some, but not all types, of electromagnetic radiation penetrates easily through the Earth's atmosphere, depending on their wavelength (see figure 3.1). This results in an optical and radio window where most radiation reaches the ground at sea level. On the Earth's surface, the radio window is approximately in the frequency range 15 MHz to a high frequency cut-off at 1.5 THz, which corresponds to approximately 20 m to 0.2 mm in the wavelength range. These numbers are not fixed as they vary with time, geographical position and altitude (Wilson et al., 2013). Mm and sub-mm astronomy is an important tool when studying the birth of stars and star formation. The mm and sub-mm range is marked in figure 3.1. Measurements in the mm and sub-mm range requires great weather and accurate antennas.
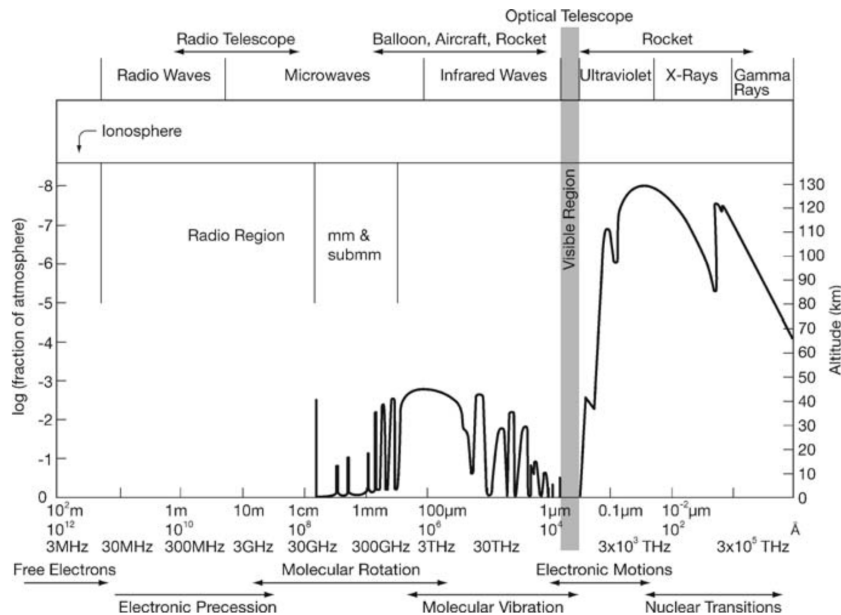


Figure 3.1: Figure illustrating the transmission of the Earth's atmosphere for electromagnetic radiation, giving the atmosphere height at which the radiation is attenuated by a factor of 1/2. Image collected from Wilson et al. (2013), p. 3.

This high frequency cut-off at 1.5 THz ($\sim$ 20 m to 0.2 mm) is caused by molecules in the troposphere, mostly water vapor, $H_2O$ and $O_2$. This is because the resonant absorption of the lowest rotation bands of these molecules fall into this frequency range. Water vapor has bands at frequencies around 22.2 GHz and 183 GHz, which corresponds to wavelength 1.35 cm and 1.63 mm respectively, and $O_2$ has a very strong band at frequency 60 GHz, corresponding to wavelength 5 mm. There are also other abundant molecules in the atmosphere that cause absorption of astronomical signals, like $N_2$ and $CO_2$, but this happens at frequencies above 300 GHz (Wilson et al., 2013).

In mm and sub-mm astronomy, effects of the troposphere are especially important. For mm and sub-mm sites, an estimation of the total amount of $H_2O$ in the atmosphere can be determined from measurements of the 183 GHz spectral line of water vapor. For sites at sea level, the 22.2 GHz spectral line of water vapor is used. The scale height, the altitude needed to go up for the quantity of e.g. water to go down by a factor of $e$, $H_{H_2O} \approx 2$ km and $H_{air} \approx 8$ km for dry air. Additionally, the water vapor in the telescope beam leads to absorption and variations in the noise input, and consequently to longer integration times for observations. This is called "sky noise" (Wilson, 2018). Therefore, it is favorable to carry out the measurements in elevated areas with a low amount of water vapor. Such places would be high, dry sites.

It is not just molecules in the atmosphere that disturbs astronomical signals, radio frequency interference (RFI) also has an impact. Man-made sources of radio signals, such as cell phones, wireless networks, satellites and garage door openers, has an increasing impact on astronomical observations. Computers and automobiles can also emit very weak signals. It is therefore beneficial to place radio telescopes in places that are sufficiently far enough away from any civilisation and man-made equipment, in addition to a dry site due to the water vapor disturbances as previously mentioned.

### 3.1.2 Radio telescopes - APEX and ALMA

The Atacama Pathfinder EXperiment (APEX), presented in figure 3.2, is an antenna with a 12-meter diameter, located on Llano de Chajnantor in the Chilean High Andes, at an altitude of 5107 meters (ESO, 2009a). The APEX antenna was a collaboration between Max Planck Institut für Radioastronomie (MPIfR), Onsala Space Observatory (OSO), and the European Southern Observatory (ESO) (Güsten et al., 2006). It operates at mm and sub-mm wavelengths between 0.2 to 1.4 mm (ESO, Accessed: 2022-04-26). The half-power beam width for APEX is

$$\theta['']= 7.8 \frac{800}{\nu[\text{GHz}]}, \tag{3.1}$$

where $\nu$ is the transition frequency.

The Atacama Large Millimeter/submillimeter Array (ALMA), presented in figure 3.3, is an astronomical interferometer consisting of 66 high-precision antennas also located in the Atacama desert in Chile, 5000 meters above sea level. The main 12-meter array has fifty antennas, where each antenna has a diameter of 12 meters, acting together as one telescope making it an interferometer. The last sixteen antennas completing ALMA is a compact array of four 12-meter and twelve 7-meter antennas. All the antennas making up ALMA can be arranged in different configurations, varying from the most compact configuration, with maximum baselines of 150 m, to the most extended configuration, with maximum baselines of 16 km. ALMA operates at wavelengths of 0.32 to 3.6 mm, studying mm and sub-mm radiation (ESO, 2013).

Figure 3.2: The APEX antenna located on the site of Llano de Chajnantor in the Chilean High Andes, at an altitude of 5107 meters. Picture taken in March 2009. Image credit: ESO (2009b).
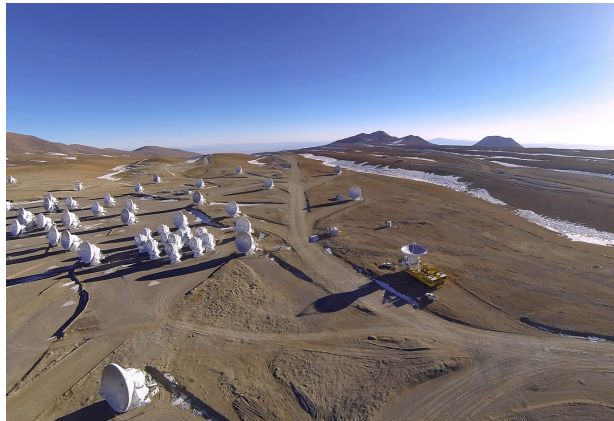


Figure 3.3: The ALMA telescope 5000 meters above sea level on the Chajnantor Plateau in the Atacama Desert of northern Chile. Image credit: A. Marinkovic/X-Cam/ALMA (ESO/NAOJ/NRAO) (ESO, 2014).

## 3.2   Spectral classes

Stars are divided into different groups based on their spectra and temperature. In the beginning of the 20th century, 7 spectral classes were developed based on absorption lines from observations, O, B, A, F, G, K, and M, where O is the hottest and M the coolest. Each of these letters were again divided into smaller groups from 0-9, where 0 is the hottest and 9 is the coolest. This system is called Harvard Spectral Classification (HSC) (Physics & Universe, 2013).

O-type stars are blue and violet giants and super giants that are extremely luminous with a high mass, and most of their radiated output is in the ultraviolet range. O-type stars are typically the first to leave the main sequence due to their high mass and very hot cores burning up the H quickly. B-type stars are also very luminous blue and white giants and super giants. Class A and F describes stars on the main sequence that has a more white color, while G-type is more yellow. Our Sun is a G-type star. K-type stars are cooler than the Sun and have a color closer to orange. M-type stars are red dwarfs, red giants or super giants. Some red dwarfs are also a class K-type star. An overview of the effective temperature, main sequence-mass, -radius and -luminosity ($M_{MS}$, $R_{MS}$ and $L_{MS}$ respectively), color and share of stars in the HSC system on the main sequence are presented in table 3.1 (Habets & Heintze, 1981) (Weidner & Vink, 2010) (Las Cumbres Observatory, Accessed 2022-01-27).

The HSC system does not include stars in the beginning or end of their lifetime, so when other types of stars were discovered by new telescopes many years later, additional spectral classes were created. The extended spectral types are W, L, T, Y, C, S and D. Class W describes hot, blue emission stars. These were once included as O-type stars, but their spectra is lacking H lines in comparison. The classes L, T and Y, in order from least to most cold, describes even cooler stars than M-type stars - cool red giants and brown dwarfs. Class C and S describes cool giant carbon-stars, while the last class D is a modern classification used for white dwarfs. All these additional classes are also divided into sub classes (Britannica, Accessed 2022-01-27a) (Britannica, Accessed 2022-01-27b).

| Class | $T_{eff}$ [K] | $M_{MS}$ [$M_\odot$] | $R_{MS}$ [$R_\odot$] | $L_{MS}$ [$L_\odot$] | Color | Stars on MS [%] |
|---|---|---|---|---|---|---|
| O | > 30 000 | $\geq$ 16 | $\geq$ 6.6 | $\geq$ 30 000 | Blue and violet | 0.00003 |
| B | 10 000-30 000 | 2.1-16 | 1.8-6.6 | 25-30 000 | Blue and white | 0.13 |
| A | 7500-10 000 | 1.4-2.1 | 1.4-1.8 | 5-25 | White | 0.6 |
| F | 6000-7500 | 1.04-1.4 | 1.15-1.4 | 1.5-5 | White and yellow | 3 |
| G | 5200-6000 | 0.8-1.04 | 0.96-1.15 | 0.6-1.5 | Yellow | 7.6 |
| K | 3700-5200 | 0.45-0.8 | 0.7-0.96 | 0.08-0.6 | Orange | 12.1 |
| M | 2400-3700 | 0.08-0.45 | $\leq$ 0.7 | $\leq$ 0.08 | Red and orange | 76.5 |

Table 3.1: Overview of the effective temperature, main sequence-mass, -radius and -luminosity ($M_{MS}$, $R_{MS}$ and $L_{MS}$), color and percentage of stars in the HSC system on the main sequence (Habets & Heintze, 1981) (Weidner & Vink, 2010) (Las Cumbres Observatory, Accessed 2022-01-27).

## 3.3   Sources

In this thesis, we will look at two UV active sources, W Hydrae located in the stellar constellation Hydrae, and R Leporis located in the stellar constellation Lepus. These stars are well known AGB stars located nearby, detected with GALEX, and therefore suitable objects to observe. In addition, $^{12}CO/^{13}CO$ abundance ratios for these stars can be found in previous research and show a discrepancy with measured C ratios. These ratios will be discussed in more detail in section 6.1.

### 3.3.1   W Hydrae

W Hydrae (W Hya) is an O-rich Mira-type variable star, with a mass-loss rate of approximately $1.5 \times 10^{-7} \, M_\odot$/year located 78 pc from the Sun (Khouri et al., 2014), corresponding to approximately 254 light years. Mira variables are stars that are pulsating so their brightness fluctuates when seen from Earth, they have pulsation periods longer than 100 days and are characterized by a deep red color. W Hya has a pulsation period of 390 days and is of spectral type M (AAVSO, 2022a). W Hya is the 7th brightest star in the near-infrared J band (transmission window in the near-infrared from $1.1 \, \mu$m to $1.4 \, \mu$m) with a magnitude of -1.7, making it even brighter than Sirius. In figure 3.4, an image of W Hya and ejected molecules surrounding the star taken with ALMA is presented.
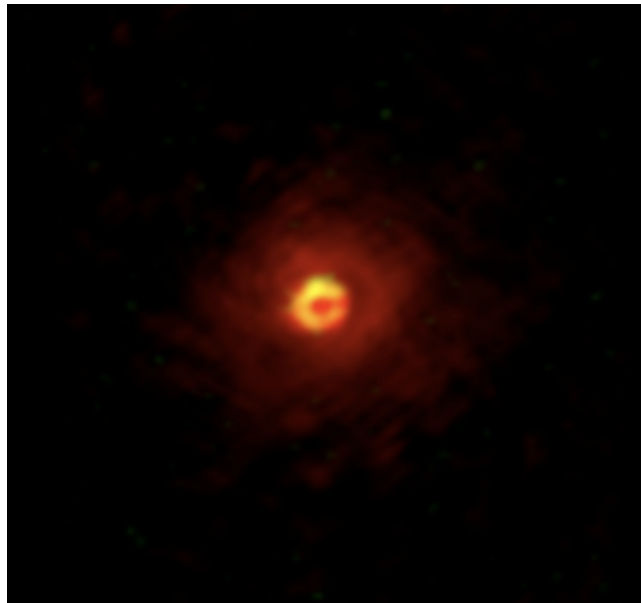


Figure 3.4: An image of W Hya showing the ejected molecules AlO (presented in red) and SiO (presented in yellow) surrounding the star. The image is taken with ALMA band 7 at wavelength $886 \, \mu$m (ESO, 2017). Credit: ALMA [ESO/NAOJ/NRAO], Takigawa et al. (2017).

### 3.3.2 R Leporis

R Leporis (R Lep) is a C-rich, class M, Mira-type variable with a huge abundance of C caused by dredge-ups. R Lep is highly evolved, very cool and radiates most of its energy through red and infrared light. In addition, the C molecules absorb what is left of blue light, causing the deep red color (NASA, 2018). It has a pulsation time of 445 days (AAVSO, 2022b) and is located at a distance of 432 pc, corresponding to approximately 1409 light years, in the stellar constellation Lepus. It has a temperature of 2200 K, luminosity of $5500\,L_\odot$ and mass-loss rate of $8.7 \times 10^{-7}\,M_\odot$/year (Danilovich et al., 2015). For lack of an image of R Lep taken with ALMA, an image of the AGB star taken by Martin Pugh (2018) is presented in figure 3.5 for illustrative purposes.



Figure 3.5: An image of R Lep taken by Martin Pugh (2018).

## 3.4 Observational data

The single-dish and interferometric observational data from the two sources, W Hya and R Lep, are collected with radio telescopes APEX and ALMA. The data reduction is conducted in CLASS (IRAM, 2022) and Python, and the data analysis is performed by use of the radiative transfer codes ALI and PRF (which will be described in more detail in section 4.1.2).

For W Hya, we look at observations of rotational transitions of molecule $H^{12}CN(J=2$-1, 3-2) at frequency 177.26 GHz for $J=2$-1 taken with APEX and 265.89 GHz for $J=3$-2 taken with ALMA, and of $H^{13}CN(J=3$-2, 4-3) at frequency 259.01 GHz for $J=3$-2 and

345.34 GHz for $J$=4-3, both taken with APEX. For R Lep we look at H$^{12}$CN ($J$=2-1, 10-9) at frequency 177.26 GHz for $J$=2-1 taken with APEX and 885.97 GHz for $J$=10-9 taken with ALMA, and at H$^{13}$CN($J$=3-2, 4-3) at 259.01 GHz for $J$=3-2 and 345.34 GHz for $J$=4-3, both taken with APEX. All the frequencies are collected from Splatalogue (2022). An overview of the different sources, the observed transitions and corresponding frequencies and energies of the upper level are presented in table 3.2. As mentioned in section 2.4, different transitions are observed from different parts of the CSE, both inner and outer. It is therefore beneficial to use observations of several transitions in order to probe the whole CSE.

| Source | Molecule | Transition $J$ | Freq [Ghz] | Telescope | $E_u$ [K] | Beam [arcsec] |
|--------|----------|----------------|------------|-----------|-----------|---------------|
| W Hya (Oxygen) | H$^{12}$CN | 2-1 | 177.26 | APEX | 12.76 | 35 |
| | | 3-2 | 265.89 | ALMA | 25.52 | 5 |
| | H$^{13}$CN | 3-2 | 259.01 | APEX | 24.86 | 24 |
| | | 4-3 | 345.34 | APEX | 41.43 | 18 |
| R Lep (Carbon) | H$^{12}$CN | 2-1 | 177.26 | APEX | 12.76 | 35 |
| | | 10-9 | 885.97 | ALMA | 233.89 | 2 |
| | H$^{13}$CN | 3-2 | 259.01 | APEX | 24.86 | 24 |
| | | 4-3 | 345.34 | APEX | 41.43 | 18 |

Table 3.2: Sources and molecules observed with APEX and ALMA, together with transitions, corresponding frequencies and energies of the upper level. Frequencies and energies are collected from Splatalogue (2022).

The reason why we are not looking at UV data as well is because we do not have UV spectra for all sources. Furthermore, these sources are very dusty, and we do not know how much dust there is, which makes it hard to find the initial UV radiation as it gets absorbed by the dust (see section 2.3.1).

# Chapter 4

# Method

By use of observational data, it is possible to explore AGB stars and CSEs with the aim of increasing our knowledge about the CSE chemistry, the mass-loss rate, the AGB stellar evolution and the effects of UV radiation. As explained in section 2.3.1, it is of great interest to look at the $H^{12}CN/H^{13}CN$ abundance ratio since this might be a more suitable tracer than the $^{12}CO/^{13}CO$ ratio for the $^{12}C/^{13}C$ ratio in UV irradiated regions in CSEs. With this goal in mind, analysis of observational data by use of rotational spectroscopy and RT is beneficial in order to find $H^{12}CN/H^{13}CN$ abundance ratios. In this section, we explain how the observations of $H^{12}CN$ and $H^{13}CN$ lines are used to look at rotational transitions, and how the data is reduced and analysed. In addition, a brief description of how to create functional files for the RT code used when analysing the data is given, and how to calculate the uncertainty between the model and data is presented. By doing this, values providing a good fit between models and data are found, including the initial abundance values which is used to calculate the $H^{12}CN/H^{13}CN$ abundance ratios. Lastly, how to calculate the HCN ratios is explained.

## 4.1   Modelling

We have received observations of several rotational transitions of $H^{12}CN$ and $H^{13}CN$ lines for two different sources, W Hya and R Lep. In order to be able to interpret these observations, an RT code will be used, solving the RT equations, presented in section 2.5, by use of accelerated lambda iterations.

### 4.1.1   Accelerated lambda iteration

The accelerated lambda iteration is a numerical scheme which is helpful when modelling, amongst other things, stellar atmospheres. The idea behind this method is to use an operator like the exact lambda operator $\Lambda_\nu$, producing an angle averaged intensity $J_\nu$ and a source function $S_\nu$ (2.14), but more approximate than exact, called $\Lambda^*$. By doing so, it allows implementations that are very fast and also sufficiently precise. The exact

lambda operator is split up and defined by use of $\Lambda^*$,

$$\Lambda_\nu = \Lambda^* + (\Lambda_\nu - \Lambda^*), \tag{4.1}$$

giving a mean intensity

$$J_\nu = \Lambda^*[S] + (\Lambda_\nu - \Lambda^*)[S], \tag{4.2}$$

that is still exact because it is defined by use of lambda operators, which operate upon the source function.

The classical lambda iteration is

$$S^{(n+1)} = (1 - \epsilon)\Lambda[S^{(n)}] + \epsilon B, \tag{4.3}$$

where $n$ is the iteration step, $\epsilon$ is the destruction probability per extinction for coherently scattering two-level atoms defined as

$$\epsilon_\nu \equiv \frac{\alpha_\nu^a}{\alpha_\nu^a + \alpha_\nu^s}, \tag{4.4}$$

where $\alpha_\nu^a$ is the partial extinction coefficient when absorption is used for extinction and $\alpha_\nu^s$ is when scattering is used, and $B$ is the Planck's law

$$B(\nu, T) = \frac{2h\nu^3}{c^2} \frac{1}{\frac{h\nu}{ek_B T} - 1}, \tag{4.5}$$

where $\nu$ is the frequency, $T$ is the temperature, $k_B$ is the Boltzmann constant, $h$ is the Planck constant and $c$ is the speed of light in the medium.

The classical lambda iteration can then for the case of two-level atoms with coherent scattering be written as

$$S^{(n+1)} = (1 - \epsilon)\Lambda^*[S^{(n+1)}] + (1 - \epsilon)(\Lambda_\nu - \Lambda^*)[S^{(n)}] + \epsilon B. \tag{4.6}$$

Moving the first term on the right hand side to the left hand side and reshuffling equation (4.6) gives

$$
\begin{aligned}
S^{(n+1)} - (1 - \epsilon)\Lambda^*[S^{(n+1)}] &= (1 - \epsilon)\Lambda_\nu[S^{(n)}] + \epsilon B - (1 - \epsilon)\Lambda^*[S^{(n)}] \\
&= S^{\text{FS}} - (1 - \epsilon)\Lambda^*[S^{(n)}],
\end{aligned} \tag{4.7}
$$

where $S^{\text{FS}} \equiv (1 - \epsilon)\Lambda_\nu[S^{(n)}] + \epsilon B$ is defined as the formal solution. Further, the new estimate is found from inverting and gives

$$S^{(n+1)} = (1 - (1 - \epsilon)\Lambda^*)^{-1}[S^{\text{FS}} - (1 - \epsilon)\Lambda^*[S^{(n)}]]. \tag{4.8}$$

The convergence speed is given by the change per step,

$$S^{(n+1)} - S^{(n)} = (1-\epsilon)\Lambda_\nu[S^{(n)}] + \epsilon B - S^{(n)}, \tag{4.9}$$

which by inserting for $S^{\text{FS}}$ then gives the convergence,

$$S^{(n+1)} - S^{(n)} = S^{\text{FS}} - S^{(n)}. \tag{4.10}$$

Then, by subtracting $S^{(n)}$ from both sides of equation (4.7) and some re-ordering, an expression for the accelerated lambda iteration is obtained

$$S^{(n+1)} - S^{(n)} = (1 - (1-\epsilon)\Lambda^*)^{-1}[S^{\text{FS}} - S^{(n)}]. \tag{4.11}$$

Further information about the accelerated lambda iteration can be found in Rutten, R. J. (2003).

### 4.1.2 Radiative transfer analysis

In this thesis, we will be using a code package named ALI (Accelerated Lambda Iteration program) and PRF written in code language $C$, modelling molecular emission lines in a CSE. ALI performs RT calculations by use of accelerated lambda iterations and PRF produces a modelled spectral line, based on the CSE models ALI generates, of a rotational transition between two energy levels for either $H^{12}CN$ or $H^{13}CN$. A benefit to using accelerated lambda iterations in our case where we look at HCN lines, as opposed to using e.g. the Monte Carlo method, is that convergence is reached quicker with the ALI method. A total description of necessary input values, how the different input files are written and how to run ALI and PRF can be found in Danilovich (2016). The goal is to find a good fit between the observed data and the modelled molecular emission lines. We assume that the CSE is spherical symmetric, that the mass loss $\dot{M}$ is constant and that the envelope expands with an expansion velocity $v_\infty$.

In order to run ALI, the first step is to write an input file containing stellar parameters and other necessary values, including the CSEs geometry, its minimum radius $R_{\min}$ in cm, its maximum radius $R_{\max}$ in cm, the temperature of the star $T^*$ in K, initial abundance $f_0$ at the inner radius, and e-folding radius $R_e$ in cm, the radius at which the initial abundance has dropped by a factor of $e$. To efficiently find a good fit between the model and data, it is useful to create a grid with several input files containing different values of the initial abundance $f_0$ and e-folding radius $R_e$, and the value for $R_{\max} = 3 \times R_e$ for each iteration. We do not expect the initial abundance, originating from the stellar photosphere, to change from star to star. This is why we can test different e-folding radii when trying to find the best fit. Our results can still be compared with previous research.

R Lep is a C-rich star, which means that it contains a relatively high amount of HCN. We therefore have to look at $H^{13}CN$, the less abundant isotopologue which is optically thin, when determining $R_e$ for this star. The way we do this is to first assume

that the e-folding radius is the same for $H^{12}CN$ as for $H^{13}CN$, as the main thing that determines the e-folding radius is the photodissociation by UV radiation, and if two molecules are affected equally by the UV radiation then we would expect them to have the same e-folding radius. Then, after a good fit between the model and data is found for $H^{13}CN$ using a 2D grid, we run a 1D grid for $H^{12}CN$ with the best $R_e$ from $H^{13}CN$, only varying $f_0$. For W Hya, which is an O-rich star and contains less HCN in general, we can derive the $R_e$ from $H^{12}CN$ if the line is optically thin. In this case, we run two separate 2D grids for each molecule and look at the results when determining the best $R_e$ value for this star.

When choosing a suitable molecular abundance distribution, set via a function, a basic Gaussian model is used for both molecules and sources,

$$f(r) = f_0 \ e^{-(\frac{r}{R_e})^\alpha}, \tag{4.12}$$

where $f(r)$ is the fractional abundance ratio of the molecule we want to look at relative to $H_2$ at each radius $r$, $f_0$ is the initial abundance, and since we have a Gaussian model, $\alpha = 2$.

When calculating the temperature, we parameterize the radial structure of the kinetic temperature $T_{\mathrm{kin}}$ and the dust temperature $T_d$ by use of power laws of type:

$$T_{\mathrm{kin}} = T_* \left(\frac{r}{R_*}\right)^{-\epsilon}, \tag{4.13}$$

$$T_{\mathrm{d}} = T_d(r_c)\left(\frac{r}{r_c}\right)^{-\epsilon_{\mathrm{d}}}, \tag{4.14}$$

where $T_*$ and $R_*$ are the stellar temperature and radius respectively and $r_c$ is the condensation radius (Massalkhi et al., 2018). We use values for $\epsilon$ and $\epsilon_{\mathrm{d}}$ from Massalkhi et al. (2018) for R Lep. For W Hya, the commonly used value for $\epsilon$, 0.65, is used, and the $\epsilon_{\mathrm{d}}$ value used is from Khouri et al. (2014). These values are presented together with other necessary input parameters in table 4.1.

After the ALI code has run, several files are written to disk. For every input file, a .pop, .log, .cool and .prf file is created. These outputs are then interpreted by use of PRF. In order to run PRF, another simpler input file needs to be written, which must have the same name as the ALI input file, but is placed in a separate folder, including the number of transition lines, the telescope beamwidths in arcseconds for each observation (3.1) and the list of transition lines. The beams are presented in table 3.2. Once PRF has run, .log files are generated, including values for velocity and line intensity, which is later extracted and used to create plots of the modelled emission lines by use of codes written in Python.

It is also necessary to create input files in a third separate folder where all the plotting scripts are located, also with the same name as the input files in the ALI and PRF

folders. This file needs to include the .dat files created by use of CLASS, containing information about the spectral line data, in order to plot the comparison between the data and the calculated model.

The required input values for the different input files are presented in table 4.1. The values for R Lep are collected from Danilovich et al. (2015) and Massalkhi et al. (2018). In addition, by exploring different ranges for $T_{kin}$, $T_d$ and $R_{min}$ for this source, the best-fitting values are found. The values used for W Hya are collected from Khouri et al. (2014). By exploring different ranges for $T_d$, $\epsilon$, $\tau_{dust}$ and $R_{min}$ for this source, the best-fitting values are found.

|  |  | W Hya | R Lep |
|---|---|---|---|
| $v_\infty$ | [km/s] | 6.5 [K] | 18 [D] |
| $v_{LSR}$ | [km/s] | 40.4 [K] | 11 [D] |
| Distance | [pc] | 78 [K] | 432 [D] |
| $L_*$ | [$L_\odot$] | 5400 [K] | 5500 [D] |
| $T_*$ | [K] | 2500 [K] | 2200 [D] |
| $\dot{M}$ | [$M_\odot/yr$] | $1.5 \times 10^{-7}$ [K] | $8.7 \times 10^{-7}$ [D] |
| $T_d$ | [K] | 2500 | 1400 |
| $T_{kin}$ | [K] | 2500 [K] | 1000 |
| $R_{min}$ | [cm] | $1 \times 10^{14}$ | $1.7 \times 10^{14}$ |
| $\epsilon_d$ |  | 0.65 [K] | 0.4 [M] |
| $\epsilon$ |  | 0.65 | 0.7 [M] |
| $\tau_{dust}$ |  | 0.1 | 0.06 [D] |

Table 4.1: Values used when creating the different input files and running ALI, PRF and visualising the results by plotting the spectral lines together with the calculated model. [K]: Khouri et al. (2014), [D]: Danilovich et al. (2015) and [M]: Massalkhi et al. (2018). For R Lep, by exploring different ranges, the best-fitting $T_{kin}$, $T_d$ and $R_{min}$ are determined. For W Hya, by exploring different ranges, the best-fitting $T_d$, $\epsilon$, $\tau_{dust}$ and $R_{min}$ are determined.

In addition to the mass-loss rate, $\dot{M}$, for W Hya presented in the table above, it is interesting to try $\dot{M} = 8 \times 10^{-8}$ (Ramstedt et al., 2020). We want to investigate how the change in mass-loss rate affects the results, compare, and observe which one is better. This is done in the same way as for W Hya with $\dot{M} = 1.5 \times 10^{-7}$, by running two 2D grids for each molecule and determining the best $R_e$ values when looking at the results.

### 4.1.3 Calculation of $\chi^2$

In order to determine the value of $f_0$ and $R_e$ that gives the best fit between the model and observations, it is helpful to look at a measurement of uncertainty between model and data, $\chi^2$. The $\chi^2$ is calculated by use of the total intensity from the model results

and the observations, and an uncertainty $\sigma$ of the observations, where 20% of the total observed flux is considered as uncertainty for all the transitions (typically used error bars for APEX observations). The $\chi^2$ is defined as follows,

$$\chi^2 = \frac{(I_{model} - I_{obs})^2}{\sigma^2}, \tag{4.15}$$

where $\sigma = 0.2 \times I_{obs}$. Another favorable trait by creating several input files with different $f_0$ and $R_e$ values is that a contour plot can be created. After the calculations are done, a contour plot of $\chi^2$ in the $f_0 - R_e$ plane is produced, visualising the $1\sigma$, $2\sigma$, $3\sigma$ and $4\sigma$ areas, where the confidence interval is 68.3%, 95.4%, 99.7% and 99.9% respectively. The $f_0$ and $R_e$ values in the middle of the inner $1\sigma$ area, giving low $\chi^2$ values, are potentially the best-fitting values for both transitions.

### 4.1.4 Deriving the molecular ratios

After the $\chi^2$ values are found for the two sources, the $f_0$ values which give a small $\chi^2$, thus a good fit between the model and data, are used to calculate the abundance ratios, $H^{12}CN/H^{13}CN$. We also need to calculate the propagation of uncertainty. This is done by first using the best $f_0$ values found for each molecule to define $f$,

$$f = \frac{A}{B}, \tag{4.16}$$

where $A$ is the best $f_0$ for $H^{12}CN$ and $B$ is the best $f_0$ for $H^{13}CN$. Then we find the standard deviation, $\sigma_f$, defined as

$$\sigma_f = |f|\sqrt{\left(\frac{\sigma_A}{A}\right)^2 + \left(\frac{\sigma_B}{B}\right)^2 - 2\frac{\sigma_{AB}}{AB}}, \tag{4.17}$$

where $\sigma_A$ and $\sigma_B$ are the standard deviations for $H^{12}CN$ and $H^{13}CN$ respectively and $\sigma_{AB}$ is the covariance. The standard deviations can be determined by looking at resulting subplots, where data and models are compared, and investigate how much we can vary $f_0$ and still get a reasonable model. The last term, $2(\sigma_{AB}/AB)$, is in our case 0, as $A$ and $B$ not are lists of numbers, but two separate values. After the uncertainties are calculated, we define the $H^{12}CN/H^{13}CN$ ratio as

$$\frac{H^{12}CN}{H^{13}CN} = f \pm \sigma_f, \tag{4.18}$$

and compare them with previously measured $^{12}CO/^{13}CO$ and $^{12}C/^{13}C$ abundance ratios.

# Chapter 5

# Results

In this section, the grid values used when performing the RT analysis and the corresponding results for the two sources are presented. First, the $f_0$ and $R_e$ values yielding small $\chi^2$ values for W Hya, thus good fits between the calculated model and observed data, are presented along with the best $\chi^2$ value, plots visualising the transition lines and the comparison between the model and data, as well as contour plots of $\chi^2$. Two additional plots using ALMA data for line $H^{12}CN(J=3\text{-}2)$ for W hya are also shown, as well as a zero-moment map. Second, the results for R Lep are presented, also visualised with subplots showing the observed transition lines together with calculated models, and a contour plot of $\chi^2$ for $H^{13}CN$. An integrated intensity plot using ALMA data and a zero-moment map for line $H^{12}CN(J=10\text{-}9)$ are presented as well. In the end, the $R_e$, $f_0$ and $\chi^2$ values giving good fits for the two sources are gathered in a table, before the $H^{12}CN/H^{13}CN$ abundance ratios for both sources are presented in a table together with $^{13}CO/^{12}CO$ and $^{13}C/^{12}C$ ratios from previous research.

## 5.1 Grid values

The different values of $f_0$ and $R_e$ ranges for R Lep and W Hya used when performing the RT analysis are presented in table 5.1. For R Lep $H^{12}CN$, the $R_e$ used is the best $R_e$ value from $H^{13}CN$.

| Source | Molecule | Mass-loss rate [$M_\odot$/yr] | $f_0$ | $R_e$ [cm] | Grid size |
|--------|----------|-------------------------------|-------|------------|-----------|
| W Hya | $H^{13}CN$ | $1.5 \times 10^{-7}$ | $[1 \times 10^{-8}, 7 \times 10^{-7}]$ | $[3 \times 10^{14}, 6 \times 10^{15}]$ | $14 \times 14$ |
| | | $8 \times 10^{-8}$ | $[1 \times 10^{-8}, 7 \times 10^{-7}]$ | $[3 \times 10^{14}, 6 \times 10^{15}]$ | $14 \times 14$ |
| | $H^{12}CN$ | $1.5 \times 10^{-7}$ | $[4 \times 10^{-7}, 5 \times 10^{-6}]$ | $[1 \times 10^{15}, 6 \times 10^{15}]$ | $10 \times 10$ |
| | | $8 \times 10^{-8}$ | $[4 \times 10^{-7}, 5 \times 10^{-6}]$ | $[1 \times 10^{15}, 6 \times 10^{15}]$ | $10 \times 10$ |
| R Lep | $H^{13}CN$ | $8.7 \times 10^{-7}$ | $[3 \times 10^{-7}, 4 \times 10^{-6}]$ | $[1 \times 10^{15}, 1 \times 10^{16}]$ | $10 \times 10$ |
| | $H^{12}CN$ | $8.7 \times 10^{-7}$ | $[3 \times 10^{-7}, 4 \times 10^{-5}]$ | $7 \times 10^{15}$ | $30 \times 1$ |

Table 5.1: Intervals for $f_0$ and $R_e$ values used to create 2D grids and 1D grid of input files to run in ALI for $H^{13}CN$ and for $H^{12}CN$.

## 5.2   W Hya

### 5.2.1   H$^{13}$CN

The H$^{13}$CN($J$=3-2, 4-3) lines for W Hya are observed with APEX. A $14 \times 14$ grid is cre-
ated for mass-loss rate $1.5 \times 10^{-7}$ (Khouri et al., 2014) using ranges given in table 5.1. A
good fit between the model and the data using $\dot{\mathrm{M}} = 1.5 \times 10^{-7}$ is when $f_0 = 1.16 \times 10^{-7}$,
$R_e = 1.56 \times 10^{15}$ and $R_{\max} = 4.67 \times 10^{15}$, giving a $\chi^2 = 8.81$. The observations of
rotational transitions $J$=3-2 and 4-3 compared with the best-fitting model using the
latter values are presented in figure 5.3. The tangential optical depth $\tau$ is $< 0.04$ for
the first line and $\tau < 0.1$ for the second. A contour plot of $\chi^2$ for H$^{13}$CN zoomed in on
the range $f_0 = [1 \times 10^{-8}, 3 \times 10^{-7}]$ and $R_e = [3 \times 10^{14}, 5 \times 10^{15}]$, in order to better see
the $1\sigma$ area, is shown in figure 5.1.

Using the ranges given in table 5.1, a $14 \times 14$ grid is also created using mass-loss rate
$\dot{\mathrm{M}} = 8 \times 10^{-8}$ (Ramstedt et al., 2020). A good fit between the model and the data using
$\dot{\mathrm{M}} = 8 \times 10^{-8}$ is when $f_0 = 1.69 \times 10^{-7}$, $R_e = 1.56 \times 10^{15}$ and $R_{\max} = 4.67 \times 10^{15}$, giving
a $\chi^2 = 6.39$. The tangential optical depth $\tau$ is $< 0.03$ for the first line and $\tau < 0.08$ for
the second. A summary of these values for both mass-loss rates are presented in table
5.2 and 5.3.

### 5.2.2   H$^{12}$CN

For the H$^{12}$CN lines we look at observations taken with both ALMA and APEX,
H$^{12}$CN($J$=2-1) with APEX and H$^{12}$CN($J$=3-2) with ALMA. A $10 \times 10$ grid is cre-
ated for the case when using mass-loss rate $\dot{\mathrm{M}} = 1.5 \times 10^{-7}$ with the ranges given in
table 5.1. A good fit between the model and the data using $\dot{\mathrm{M}} = 1.5 \times 10^{-7}$ yields
$\chi^2 = 0.05$ when $f_0 = 2.96 \times 10^{-6}$, $R_e = 1.56 \times 10^{15}$ and $R_{\max} = 4.67 \times 10^{15}$. The ob-
servations of rotational transitions $J$=2-1 and 3-2 compared with the best-fitting model
using the latter values are presented in figure 5.3. The tangential optical depth $\tau$ is
$< 0.21$ for the first line and $\tau < 0.65$ for the second. A contour plot of $\chi^2$ for H$^{12}$CN is
shown in figure 5.2.

Also for mass-loss rate $\dot{\mathrm{M}} = 8 \times 10^{-8}$, using the ranges given in table 5.1, a $10 \times 10$
grid is created. A good fit between the model and the data yields $\chi^2 = 0.23$ when
$f_0 = 5 \times 10^{-6}$, $R_e = 1.56 \times 10^{15}$ and $R_{\max} = 4.67 \times 10^{15}$. The tangential optical depth
$\tau$ is $< 0.19$ for the first line and $\tau < 0.61$ for the second. A summary of these values
for both mass-loss rates are presented in table 5.2 and 5.3.

### 5.2.3   Plots

A contour plot of $\chi^2$ for W Hya H$^{13}$CN when using $\dot{\mathrm{M}} = 1.5 \times 10^{-7}$ is presented in
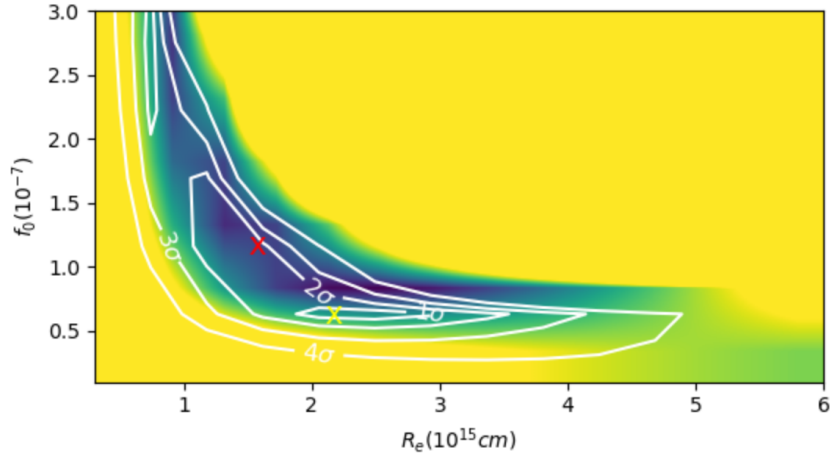figure 5.1 and for H$^{12}$CN in figure 5.2.

Figure 5.1: Contour plot of $\chi^2$ for W Hya $H^{13}CN$ zoomed in on the area $f_0 = [1 \times 10^{-8}, 3 \times 10^{-7}]$ and $R_e = [3 \times 10^{14}, 5 \times 10^{15}]$. The red cross marks the best model for $H^{13}CN$ presented in figure 5.3: $\dot{M} = 1.5 \times 10^{-7}$, $f_0 = 1.16 \times 10^{-7}$,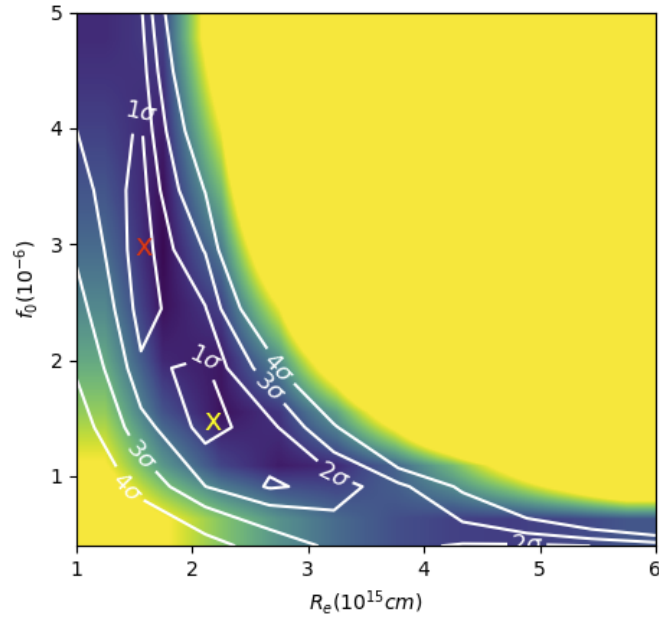 $R_e = 1.56 \times 10^{15}$ and $\chi^2 = 8.81$. The yellow cross marks the model for $H^{13}CN$ shown in figure 5.4: $\dot{M} = 1.5 \times 10^{-7}$, $f_0 = 6.31 \times 10^{-8}$, $R_e = 2.1 \times 10^{15}$ and $\chi^2 = 5.51$.



Figure 5.2: Contour plot of $\chi^2$ for W Hya $H^{12}CN$ with grid values $f_0 = [4 \times 10^{-7}, 5 \times 10^{-6}]$ and $R_e = [1 \times 10^{15}, 6 \times 10^{15}]$. The red cross marks the best model for $H^{12}CN$ presented in figure 5.3: $\dot{M} = 1.5 \times 10^{-7}$, $f_0 = 2.96 \times 10^{-6}$, $R_e = 1.56 \times 10^{15}$ and $\chi^2 = 0.05$. The yellow cross marks the model for $H^{12}CN$ shown in figure 5.4: $\dot{M} = 1.5 \times 10^{-7}$, $f_0 = 1.41 \times 10^{-6}$, $R_e = 2.1 \times 10^{15}$ and $\chi^2 = 0.88$.

The red crosses in the contour plots marks the best models using the values presented in section 5.2.1 and 5.2.2 when $\dot{M} = 1.5 \times 10^{-7}$. Plots of observed emission lines compared with these models for both molecules are presented in figure 5.3. In addition, since we observe that the contour plots share a common $1\sigma$ area using $R_e = 2.1 \times 10^{15}$, we also look at plots of emission lines compared with the best models using this $R_e$ for both molecules in order to compare. The best model for $H^{13}CN$ using $R_e = 2.1 \times 10^{15}$ is when $f_0 = 6.31 \times 10^{-8}$ giving a $\chi^2 = 5.51$, and for $H^{12}CN$ when $f_0 = 1.41 \times 10^{-6}$ and $\chi^2 = 0.88$. These plots are presented in figure 5.4 and marked with a yellow cross in the contour plots.
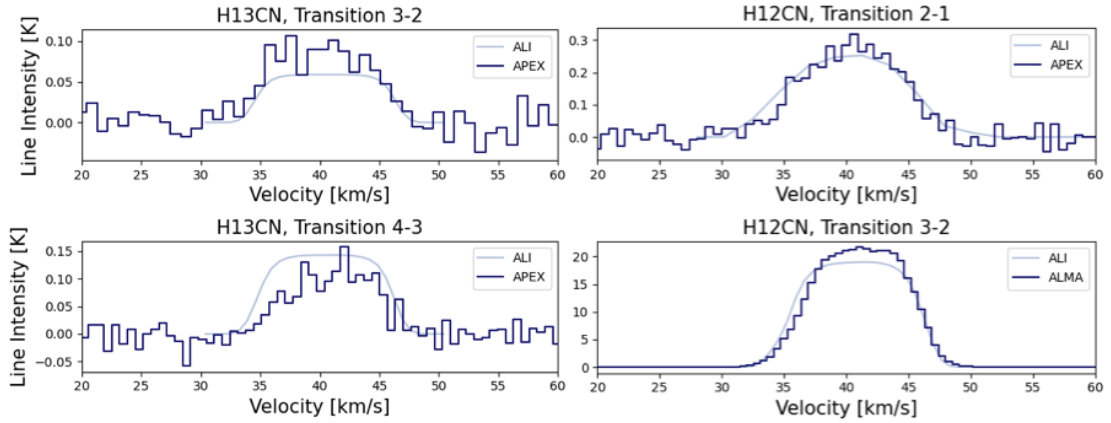


Figure 5.3: Plots for W Hya.
**To the left**: Emission lines of $H^{13}CN$ (dark blue) compared with the calculated model (light blue). $\dot{M} = 1.5 \times 10^{-7}$, $f_0 = 1.16 \times 10^{-7}$, $R_e = 1.56 \times 10^{15}$ and $\chi^2 = 8.81$. The observations for both transitions are measured with APEX.
**To the right**: Emission lines of $H^{12}CN$ (dark blue) compared with the calculated model (light blue). $\dot{M} = 1.5 \times 10^{-7}$, $f_0 = 2.96 \times 10^{-6}$, $R_e = 1.56 \times 10^{15}$ and $\chi^2 = 0.05$. The observations for $H^{12}CN(J{=}2{-}1)$ are measured with APEX and the observations for $H^{12}CN(J{=}3{-}2)$ are measured with ALMA.
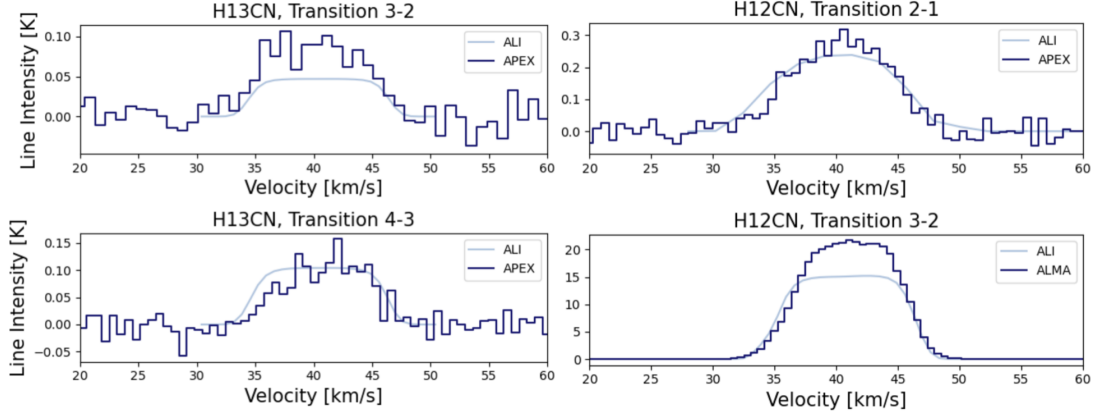
Figure 5.4: Plots for W Hya.
**To the left**: Emission lines of $H^{13}CN$ (dark blue) compared with the calculated model (light blue). $\dot{M} = 1.5 \times 10^{-7}$, $f_0 = 6.31 \times 10^{-8}$, $R_e = 2.1 \times 10^{15}$ and $\chi^2 = 5.51$. The observations for both transitions are measured with APEX.
**To the right**: Emission lines of $H^{12}CN$ (dark blue) compared with the calculated model (light blue). $\dot{M} = 1.5 \times 10^{-7}$, $f_0 = 1.41 \times 10^{-6}$, $R_e = 2.1 \times 10^{15}$ and $\chi^2 = 0.88$. The observations for $H^{12}CN(J=2\text{-}1)$ are measured with APEX and the observations for $H^{12}CN(J=3\text{-}2)$ are measured with ALMA.

Since we have spatially resolved ALMA observations of the $H^{12}CN(J=3\text{-}2)$ line for W Hya, we can directly compare the integrated intensities at radial offset points from observations with the RT model. This is presented in figure 5.5. Model 1 (red dots) and model 2 (yellow dots) corresponds to the models marked with the red cross and yellow cross in figure 5.2 respectively. Model 1, which represents the best-fitting model, has values $\dot{M} = 1.5 \times 10^{-7}$, $f_0 = 2.96 \times 10^{-6}$, $R_e = 1.56 \times 10^{15}$ and $\chi^2 = 0.05$, and is presented in the bottom right corner in figure 5.3. Model 2 has values $\dot{M} = 1.5 \times 10^{-7}$, $f_0 = 1.41 \times 10^{-6}$, $R_e = 2.1 \times 10^{15}$ and $\chi^2 = 0.88$, and is presented in the bottom right corner in figure 5.4. Figure 5.6 shows the spectra extracted from the central star corresponding to the first blue point in figure 5.5, with a circular beam of $0.18''$. Figure 5.7 shows spatially resolved ALMA observations of $H^{12}CN(J=3\text{-}2)$ towards W Hya.
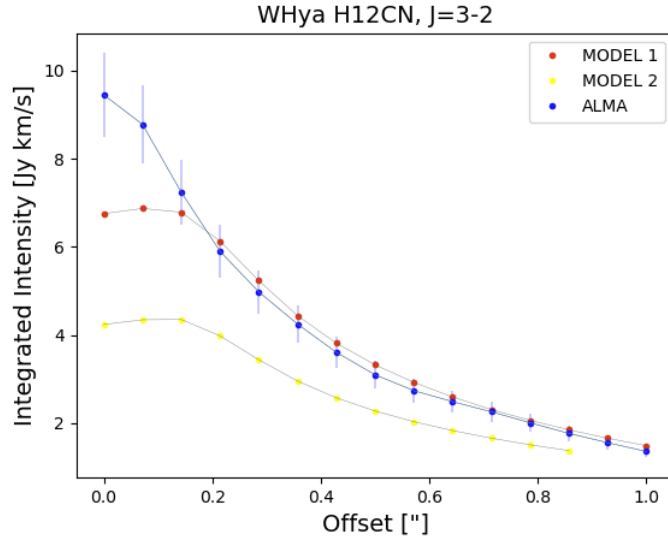
Figure 5.5: Comparison of integrated intensities of the $H^{12}CN(J$=3-2) line from ALMA observations of W Hya, at radial offset points averaged over four directions from the central star, and the results of two models from the RT analysis. Model 1 (red dots), which represents the best-fitting model, has values $\dot{M} = 1.5 \times 10^{-7}$, $f_0 = 2.96 \times 10^{-6}$, $R_e = 1.56 \times 10^{15}$ and $\chi^2 = 0.05$, and is shown in the bottom right corner in figure 5.3. Model 2 (yellow dots) has values $\dot{M} = 1.5 \times 10^{-7}$, $f_0 = 1.41 \times 10^{-6}$, $R_e = 2.1 \times 10^{15}$ and $\chi^2 = 0.88$, and is shown in the bottom right corner in figure 5.4. The error bars of the observation points (blue bars) show 10% uncertainty on flux calibration.
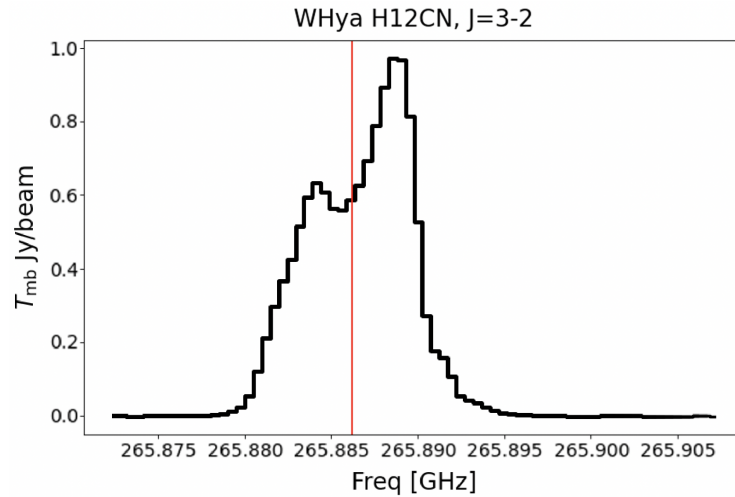


Figure 5.6: Integrated intensity of $H^{12}CN(J$=3-2) from ALMA observations towards W Hya, extracted from a beam size of $0.18''$. The red line represents the $H^{12}CN$ line (265.89 GHz).
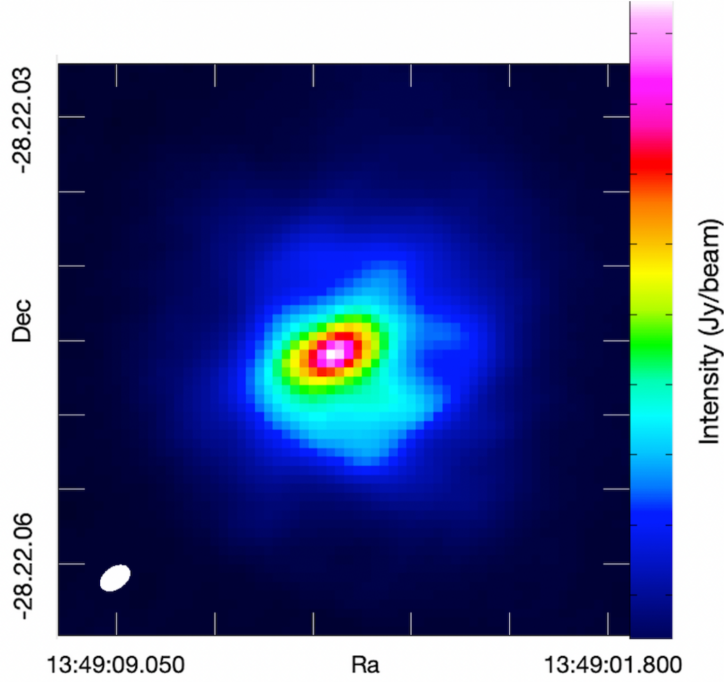
Figure 5.7: Zero-moment H$^{12}$CN($J$=3-2) map of W Hya observed with ALMA. The ALMA beam size is shown in the bottom left corner (0.18″).

## 5.3 R Lep

### 5.3.1 H$^{13}$CN

The H$^{13}$CN($J$=3-2, 4-3) lines for R Lep are observed with APEX. A $10 \times 10$ grid is created with the ranges given in table 5.1. A good fit between the model and the data yields $\chi^2 = 7.98$ when $f_0 = 7.11 \times 10^{-7}$, $R_e = 7 \times 10^{15}$ and $R_{\max} = 2.1 \times 10^{16}$. A subplot showing the two transitions for H$^{13}$CN compared with the calculated model is presented in figure 5.8. The tangential optical depth $\tau$ is $< 0.43$ for the first line and $\tau < 0.84$ for the second. In addition, a contour plot of $\chi^2$ for H$^{13}$CN is shown in figure 5.9. A summary of these values are presented in table 5.2 and 5.3.

### 5.3.2 H$^{12}$CN

The H$^{12}$CN observations are taken with both ALMA and APEX, H$^{12}$CN($J$=2-1) with APEX and H$^{12}$CN($J$=10-9) with ALMA. When searching for a good fit for H$^{12}$CN, we run a 1D grid with the $R_e$ value giving the best fit for H$^{13}$CN, $R_e = 7 \times 10^{15}$, and $f_0 = [3 \times 10^{-7}, 4 \times 10^{-5}]$. A good fit between the model and the data yields $\chi^2 = 11.07$ when $f_0 = 2.5 \times 10^{-5}$, $R_e = 7 \times 10^{15}$ and $R_{\max} = 2.1 \times 10^{16}$. A plot presenting the two transitions for H$^{12}$CN compared with the calculated model is shown in figure 5.8.

The tangential optical depth $\tau$ is $< 0.91$ for the first line and $\tau < 8.4$ for the second. A summary of these values are presented in table 5.2 and 5.3.

### 5.3.3 Plots

Plots of observed emission lines compared with the best models for both molecules are presented in figure 5.8. The $\chi^2$ contour plot for $H^{13}CN$ is presented in figure 5.9.

We also have spatially resolved ALMA observations of the $H^{12}CN(J{=}10{-}9)$ line for R Lep. Thus we can directly compare the integrated intensities at radial offset points from observations with the RT model. This is presented in figure 5.10. As shown, our best model (red dots) for the $H^{12}CN(J{=}10{-}9)$ line is in great agreement with the ALMA observations. The best model (red dots) has values $f_0 = 2.5 \times 10^{-5}$, $R_e = 7 \times 10^{15}$ and $\chi^2 = 11.07$, and is presented in the bottom right corner in figure 5.8. Figure 5.11 shows spatially resolved ALMA observations of $H^{12}CN(J{=}10{-}9)$ towards R Lep.
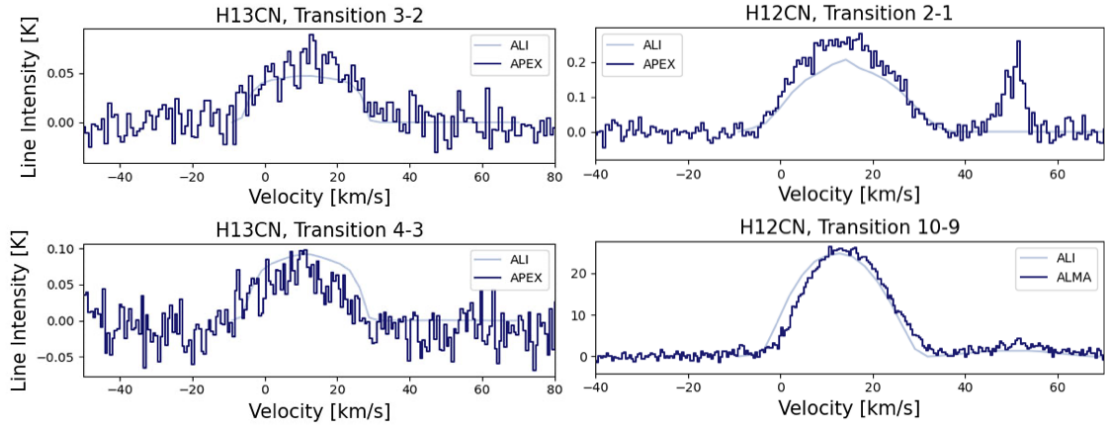


Figure 5.8: Plots for R Lep.
**To the left**: Emission lines of $H^{13}CN$ (dark blue) compared with the calculated model (light blue). $f_0 = 7.11 \times 10^{-7}$, $R_e = 7 \times 10^{15}$ and $\chi^2 = 7.98$. The observations for both transitions are measured with APEX.
**To the right**: Emission lines of $H^{12}CN$ (dark blue) compared with the calculated model (light blue). $f_0 = 2.5 \times 10^{-5}$, $R_e = 7 \times 10^{15}$ and $\chi^2 = 11.07$. The observations for $H^{12}CN(J{=}2{-}1)$ are measured with APEX and the observations for $H^{12}CN(J{=}10{-}9)$ are measured with ALMA.
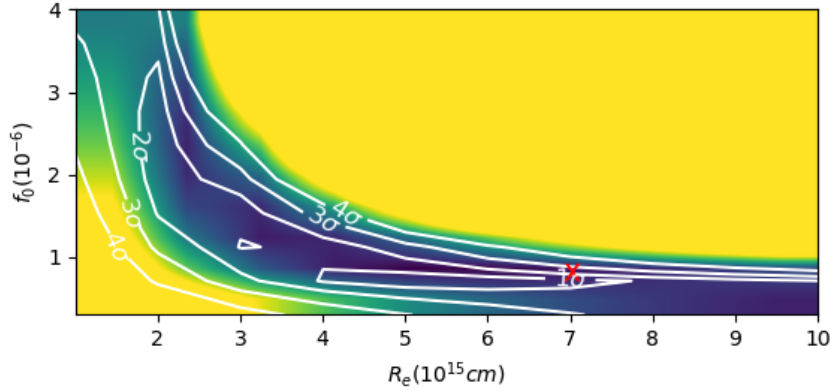
Figure 5.9: Contour plot of $\chi^2$ for R Lep H$^{13}$CN with grid values $f_0 = [3 \times 10^{-7}, 4 \times 10^{-6}]$ and $R_e = [1 \times 10^{15}, 1 \times 10^{16}]$. The red cross marks the best model for H$^{13}$CN presented in figure 5.8: $f_0 = 7.11 \times 10^{-7}$, $R_e = 7 \times 10^{15}$ and $\chi^2 = 7.98$.
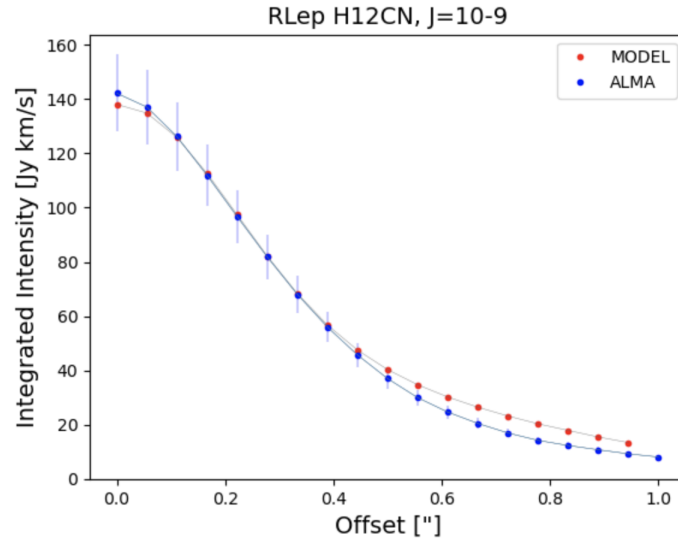


Figure 5.10: Comparison of integrated intensities of the H$^{12}$CN($J$=10-9) line from ALMA observations of R Lep, at radial offset points averaged over four directions from the central star, and the result of the best-fitting model from the RT analysis. The best model (red dots) has values $f_0 = 2.5 \times 10^{-5}$, $R_e = 7 \times 10^{15}$ and $\chi^2 = 11.07$, and is shown in the bottom right corner in figure 5.8. The error bars of the observation points (blue bars) show 10% uncertainty on flux calibration.
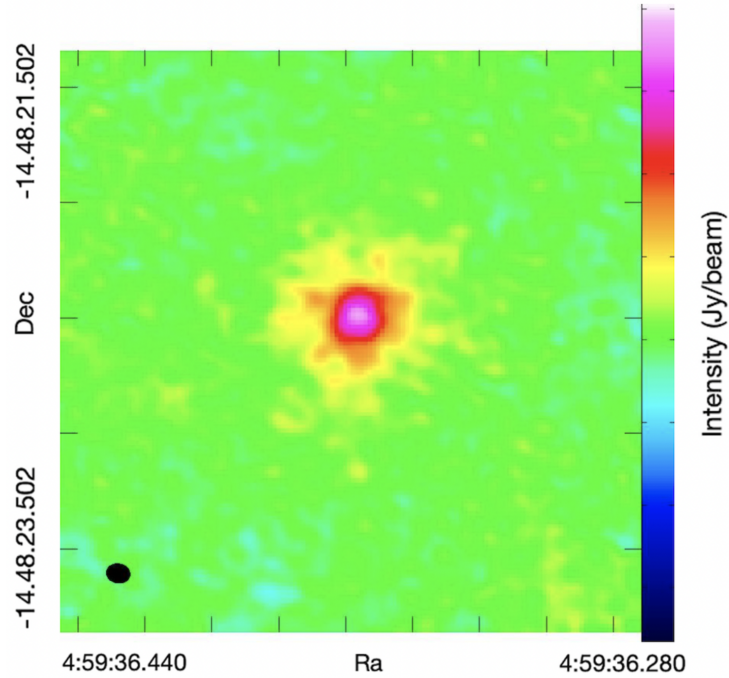
Figure 5.11: Zero-moment H$^{12}$CN($J$=10-9) map of R Lep observed with ALMA. The ALMA beam size is shown in the bottom left corner (0.09$''$).

## 5.4    Molecular ratios

The values yielding the best fits between the models and data for H$^{12}$CN and H$^{13}$CN for both sources are presented below in table 5.2. For W Hya when using $\dot{\text{M}} = 1.5 \times 10^{-7}$, we choose values for both molecules from the models presented in figure 5.3. We see when comparing figure 5.3 to figure 5.4 that the models for both molecules overall fit the data better in figure 5.3. An overview of the largest tangential optical depths, $\tau$, for every rotational transition $J$ is shown in table 5.3.

| Source | Molecule | Mass-loss rate [M$_\odot$/yr] | $f_0$ | $R_e$ [cm] | Smallest $\chi^2$ |
|--------|----------|------------------------------|-------|-----------|------------------|
| W Hya | H$^{13}$CN | $1.5 \times 10^{-7}$ | $1.16 \times 10^{-7}$ | $1.56 \times 10^{15}$ | 8.81 |
|  |  | $8 \times 10^{-8}$ | $1.69 \times 10^{-7}$ | $1.56 \times 10^{15}$ | 6.39 |
|  | H$^{12}$CN | $1.5 \times 10^{-7}$ | $2.96 \times 10^{-6}$ | $1.56 \times 10^{15}$ | 0.05 |
|  |  | $8 \times 10^{-8}$ | $5 \times 10^{-6}$ | $1.56 \times 10^{15}$ | 0.23 |
| R Lep | H$^{13}$CN | $8.7 \times 10^{-7}$ | $7.11 \times 10^{-7}$ | $7 \times 10^{15}$ | 7.98 |
|  | H$^{12}$CN | $8.7 \times 10^{-7}$ | $2.5 \times 10^{-5}$ | $7 \times 10^{15}$ | 11.07 |

Table 5.2: Values for $f_0$, $R_e$ and $\chi^2$ giving good fits between the models and data for H$^{13}$CN and H$^{12}$CN for both sources.

| Source | Molecule | Mass-loss rate [$M_\odot$/yr] | Transition $J$ | Biggest $\tau$ |
|---|---|---|---|---|
| W Hya | H$^{13}$CN | $1.5 \times 10^{-7}$ | 3-2 | 0.04 |
| | | | 4-3 | 0.1 |
| | | $8 \times 10^{-8}$ | 3-2 | 0.03 |
| | | | 4-3 | 0.08 |
| | H$^{12}$CN | $1.5 \times 10^{-7}$ | 2-1 | 0.21 |
| | | | 3-2 | 0.65 |
| | | $8 \times 10^{-8}$ | 2-1 | 0.19 |
| | | | 3-2 | 0.61 |
| R Lep | H$^{13}$CN | $8.7 \times 10^{-7}$ | 3-2 | 0.43 |
| | | | 4-3 | 0.84 |
| | H$^{12}$CN | $8.7 \times 10^{-7}$ | 2-1 | 0.91 |
| | | | 10-9 | 8.4 |

Table 5.3: An overview of the biggest tangential optical depths, $\tau$, for every rotational transition $J$ for both sources.

The abundance values, $f_0$, presented in table 5.2 are used to find the H$^{12}$CN/H$^{13}$CN abundance ratios for the two sources. These are 25±14 for W Hya using $\dot{M} = 1.5 \times 10^{-7}$, 29±9 when using $\dot{M} = 8 \times 10^{-8}$, and 35±11 for R Lep using $\dot{M} = 8.7 \times 10^{-7}$. These ratios are presented in table 5.4 together with the $^{12}$CO/$^{13}$CO abundance ratios collected from Khouri et al. (2014), using $\dot{M} = 1.5 \times 10^{-7}$ for W Hya, and from Ramstedt & Olofsson (2014), using $\dot{M} = 7 \times 10^{-7}$ for R Lep and $\dot{M} = 1.5 \times 10^{-7}$ for W Hya. In addition, the $^{12}$C/$^{13}$C abundance ratios collected from Hinkle et al. (2016) for both sources are presented in the table as well. The mass-loss rates used to derive the $^{12}$C/$^{13}$C abundance ratios are unknown. Further information about the CO and C ratios are presented in section 6.1.

| Source | $^{12}$CO/$^{13}$CO | $^{12}$C/$^{13}$C | H$^{12}$CN/H$^{13}$CN |
|---|---|---|---|
| W Hya | $18 \pm 10$ [K] | $16 \pm 4$ [H] | $25 \pm 14$ [$\dot{M}_1$] |
| | $10$ [R] | | $29 \pm 9$ [$\dot{M}_2$] |
| R Lep | $22$ [R] | $34 \pm 5$ [H] | $35 \pm 11$ [$\dot{M}_3$] |

Table 5.4: Previously measured $^{12}$CO/$^{13}$CO and $^{12}$C/$^{13}$C abundance ratios together with H$^{12}$CN/H$^{13}$CN abundance ratios found by use of $f_0$ values presented in table 5.2. [R]: Ramstedt & Olofsson (2014), [K]: Khouri et al. (2014), [H]: Hinkle et al. (2016), [$\dot{M}_1$]: using $f_0$ found by use of $\dot{M} = 1.5 \times 10^{-7}$, [$\dot{M}_2$]: using $f_0$ found by use of $\dot{M} = 8 \times 10^{-8}$, [$\dot{M}_3$]: using $f_0$ found by use of $\dot{M} = 8.7 \times 10^{-7}$.

# Chapter 6

# Discussion and conclusion

In this thesis, we have modelled CSEs around two UV active AGB stars, W Hydrae and R Leporis, and performed radiative transfer analysis of observed $H^{12}CN$ and $H^{13}CN$ lines. For both sources and molecules, we present subplots visualising the observed emission lines compared with a calculated model which fits the data well, in addition to contour plots of $\chi^2$. Plots and maps for both sources using ALMA data are presented as well. We then use the abundance values from the best-fitting models to derive the $H^{12}CN/H^{13}CN$ abundance ratios for both sources and compare them to previously measured $^{12}CO/^{13}CO$ and $^{12}C/^{13}C$ ratios.

## 6.1 $^{12}CO/^{13}CO$ and $^{12}C/^{13}C$ ratios

When deriving the $^{12}CO/^{13}CO$ abundance ratio for W Hya, Ramstedt & Olofsson (2014) look at rotational transitions $J$=1-0, 2-1, 3-2, 4-3 and 6-5 for $^{12}CO$ and $J$=6-5 for $^{13}CO$. For R Lep, they look at rotational transitions $J$=1-0, 2-1 and 3-2 for $^{12}CO$ and $J$=1-0 and 2-1 for $^{13}CO$. They report a CO ratio of 10 for W Hya and 22 for R Lep. These ratios are found by use of radiative transfer analysis of single-dish radio line emission observations. In order to ensure that a large extent of the CSE is probed, they observe several different transitions. The RT model used is based on the Monte Carlo method and solves the SE equations in full non-local thermodynamic equilibrium (non-LTE), as it assumes that the radiation field is non-local. The effects of thermal dust radiation are taken into account, and the equation determining the gas temperature distribution is solved self-consistently. The way the ratios are calculated is to first solve the RT equations for $^{12}CO$ assuming an abundance based on the chemical type of the star, then solve for $^{13}CO$ using the results of the $^{12}CO$ model, giving the $^{13}CO$ initial abundance. In the end, the $^{12}CO/^{13}CO$ abundance ratio is determined. They also derive a $^{12}CO/^{13}CO$ ratio from the line intensities and find that the $^{12}CO/^{13}CO$ ratio for W Hya($J$=6-5) is $9.6/1.1 \approx 9$ and $18.1/0.5 \approx 36$ for R Lep($J$=2-1), but we compare the resulting $H^{12}CN/H^{13}CN$ ratios with the CO ratios derived by use of the RT model as this is the same method we use.

Khouri et al. (2014) derive a $^{12}$CO/$^{13}$CO ratio of 18±10 for W Hya. They look at rotational transitions $J$=6-5, 9-8 and 10-9 for $^{13}$CO and a range from $J$=1-0 to $J$=30-29 for $^{12}$CO. When modelling the $^{12}$CO and $^{13}$CO emission lines, they combine a non-LTE molecular excitation and RT code with a Monte Carlo dust continuum RT code (used to calculate the dust temperature). By combining these methods, the gaseous and dusty components of the CSE are given a consistent physical description. They also assume spherical symmetry and a constant mass-loss rate.

Hinkle et al. (2016) report $^{12}$C/$^{13}$C ratios of 16±4 and 34±5 for W Hya and R Lep respectively. The method used to obtain the C abundance ratios is to measure vibration-rotation first and second-overtone CO lines in the 2.3-2.5 $\mu$m and 1.5-1.8 $\mu$m regions and then derive the ratios. The reduction techniques used are as in Hinkle et al. (1976), Hinkle et al. (1982) and Hinkle (1978), a simple curve-of-growth (CoG) technique. This method is used to derive elemental abundances and is a powerful method if only isotopic ratios are derived. Many simplifying assumptions are made, but these can be dealt with through spectrum synthesis. By measuring the shift between different curves when plotting CoGs for near-infrared first- and second-overtone lines derived from measurements of various CO isotopologues, the $^{12}$C/$^{13}$C isotopic ratios are determined.

## 6.2   Discussion and conclusion

As CO is destroyed by photodissociation when exposed to UV radiation, and since the $^{12}$CO molecule is more abundant than the $^{13}$CO isotopologue, thus is subject to more shielding than the $^{13}$CO isotopologue, the $^{12}$CO/$^{13}$CO ratio is affected in UV irradiated areas. The H$^{12}$CN/H$^{13}$CN ratio, which is not affected by UV radiation as the H$^{12}$CN and H$^{13}$CN molecules are equally affected, is therefore expected to be a more reliable tracer of the $^{12}$C/$^{13}$C ratio.

For R Lep, we find good matches between the data and models for both molecules (figure 5.8). In addition, we observe from figure 5.10 that our best model (represented with red dots) for the H$^{12}$CN($J$=10-9) line is in great agreement with the ALMA observations. We find an H$^{12}$CN/H$^{13}$CN ratio of 35±11. This HCN abundance ratio is consistent with the $^{12}$C/$^{13}$C ratio of 34±5 (Hinkle et al., 2016), indicating that the H$^{12}$CN/H$^{13}$CN abundance ratio indeed is a good tracer for the photospheric $^{12}$C/$^{13}$C ratio in UV irradiated regions. This has also been shown in previous research by Saberi et al. (2017) for another C-rich AGB star, R Sculptoris. In addition, we also observe that our HCN ratio is a better tracer than the $^{12}$CO/$^{13}$CO ratio of 22 reported by Ramstedt & Olofsson (2014).

For W Hya, we use two different mass-loss rates from literature, as mentioned in the end of section 4.1.2, and find that the resulting two H$^{12}$CN/H$^{13}$CN ratios are 25±14 when using $\dot{\mathrm{M}} = 1.5 \times 10^{-7}$ and 29±9 when using $\dot{\mathrm{M}} = 8 \times 10^{-8}$. Ramstedt & Olofsson

(2014) and Khouri et al. (2014) report a $^{12}$CO/$^{13}$CO ratio of 10 and 18$\pm$10 respectively, while Hinkle et al. (2016) reports a $^{12}$C/$^{13}$C ratio of 16$\pm$14 for W Hya. Our results are consistent with these previously reported CO and C isotopologue ratios when the uncertainties in the final results, and the different methods and models used, are taken into account. We should note that when using $\dot{M} = 1.5 \times 10^{-7}$, the same mass-loss rate used by Khouri et al. (2014), our derived HCN ratio for W Hya is in better agreement with the CO ratio reported in this paper, than with the CO ratio reported by Ramstedt & Olofsson (2014). This analysis indicates that both the CO and HCN isotopologue ratios are consistent with the C ratio in W Hya.

As shown in figure 5.5, our best model for W Hya is in a good agreement with the observations at radial points $> 0.2''$. In the inner part, our model underestimate the intensities. This could be due to the enhancement of the gas density in the innermost region and/or the enhancement of the HCN abundance which we have not considered in our modelling, as our model aims to model the entire CSE. In addition, we speculate if the H$^{12}$CN($J$=3-2) line is blended with an unknown species in the innermost region of the CSE, as we observe that the spectra is double peaked in figure 5.6. Further investigation is needed to prove these scenarios. Considering an enhancement of the HCN abundance and/or the gas density in the inner part would be favorable.

Our results indicate that the H$^{12}$CN/H$^{13}$CN abundance ratio is consistent with the previously reported photospheric $^{12}$C/$^{13}$C ratio in the C-rich AGB star, R Lep. This suggests that the HCN isotopologue ratio can be a more reliable tracer of the photospheric C ratio in UV dominated CSEs than the previous commonly used $^{12}$CO/$^{13}$CO ratio for C-rich AGB stars, as also previously shown by Saberi et al. (2017). Our analysis for the O-rich AGB star, W Hya, predicts an HCN ratio that is in agreement with both the previously measured C and CO ratio. In future work, it would be beneficial to observe several UV active O-rich sources, measure their H$^{12}$CN/H$^{13}$CN ratios and compare with $^{12}$CO/$^{13}$CO and $^{12}$C/$^{13}$C abundance ratios. By creating a bigger collection of HCN ratios, we will be able to look at the overall trend in the comparison between H$^{12}$CN/H$^{13}$CN ratios and $^{12}$CO/$^{13}$CO and $^{12}$C/$^{13}$C ratios. This would be profitable when testing the hypothesis if the H$^{12}$CN/H$^{13}$CN ratio could be a better tracer for the photospheric $^{12}$C/$^{13}$C ratio instead of the $^{12}$CO/$^{13}$CO ratio in O-rich AGB stars.

# Bibliography

AAVSO. 2022a, VSX : Detail for W Hya. https://www.aavso.org/vsx/index.php?view=detail.top&oid=15965

—. 2022b, VSX : Detail for R Lep. https://www.aavso.org/vsx/index.php?view=detail.top&oid=17280

Britannica. Accessed 2022-01-27a, Wolf-Rayet star | astronomy | Britannica. https://www.britannica.com/science/Wolf-Rayet-star

—. Accessed 2022-01-27b, stellar classification | astronomy | Britannica. https://www.britannica.com/science/stellar-classification

Carroll, B. W., & Ostlie, D. A. 2014, An introduction to modern astrophysics; 2nd ed. (Edinburgh Gate, Harlow, Essex, England: Pearson Education Limited), 492–525

Cummings, J. D., Kalirai, J. S., Tremblay, P.-E., & Ramirez-Ruiz, E. 2016, The Astrophysical Journal, 818, doi: 10.3847/0004-637X/818/1/84

Danilovich, T. 2016, How to use MCP, ALI and PRF - A radiative transfer package for modelling molecular emission lines

Danilovich, T., Teyssier, D., Justtanont, K., et al. 2015, Astronomy & Astrophysics, 581, A60, doi: 10.1051/0004-6361/201526705

Decin, L., De Beck, E., Brünken, S., et al. 2010, Astronomy & Astrophysics, 516, A69, doi: 10.1051/0004-6361/201014136

ESO. 2007, Hertzsprung-Russell Diagram. https://www.eso.org/public/images/eso0728c/

—. 2009a, APEX - Atacama Pathfinder Experiment telescope. https://www.eso.org/public/teles-instr/apex/

—. 2009b, APEX. https://www.eso.org/public/images/apex-mar2009-1678/

ESO. 2012, Surprising Spiral Structure Spotted by ALMA - New observations reveal the secrets of a dying star, https://www.eso.org/public/news/eso1239/

ESO. 2013, ALMA - Atacama Large Millimeter/submillimeter Array. https://www.eso.org/public/teles-instr/alma/

—. 2014, The final ALMA antenna arrives at Chajnantor. https://www.eso.org/public/images/ann14048a/

—. 2017, Winds blowing on a dying star. https://www.eso.org/public/images/20171102_whya/

—. Accessed: 2022-04-26, Telescopes and Instrumentation. https://www.eso.org/public/teles-instr/

Güsten, R., Nyman, L. Ã., Schilke, P., et al. 2006, Astronomy & Astrophysics, 454, L13, doi: 10.1051/0004-6361:20065420

Goldman, S. R., van Loon, J. T., Zijlstra, A. A., et al. 2017, Monthly Notices of the Royal Astronomical Society, 465, 403–433, doi: 10.1093/mnras/stw2708

Groenewegen, M. A. T., Sloan, G. C., Soszynski, I., & Petersen, E. A. 2009, Astronomy & Astrophysics, 506, 1277–1296, doi: 10.1051/0004-6361/200912678

Habets, G. M. H. J., & Heintze, J. R. W. 1981, Astronomy & Astrophysics, 193–237, table VII,VIII. https://adsabs.harvard.edu/full/1981A%26AS...46..193H

Habing, H., & Olofsson, H. 2003, Asymptotic Giant Branch Stars; 1st ed. (New York, NY: Springer Science+Business Media New York), 266–268

Höfner, S., & Olofsson, H. 2018, Astronomy and Astrophysics Review, 26, doi: 10.1007/s00159-017-0106-5

Hinkle, K. H. 1978, The Astrophysical Journal, 220, 210, doi: 10.1086/155897

Hinkle, K. H., Hall, D. N. B., & Ridgway, S. T. 1982, The Astrophysical Journal, 252, 18. https://articles.adsabs.harvard.edu/pdf/1982ApJ...252..697H

Hinkle, K. H., Lambert, D. L., & Snell, R. L. 1976, The Astrophysical Journal, 210, 684, doi: 10.1086/154875

Hinkle, K. H., Lebzelter, T., & Straniero, O. 2016, The Astrophysical Journal, 825, 38, doi: 10.3847/0004-637X/825/1/38

IRAM. 2022, Introduction Gildas, https://www.iram.fr/IRAMFR/GILDAS/

Jiménez-Esteban, F. M., & Engels, D. 2015, Astronomy & Astrophysics, 579, A76, doi: 10.1051/0004-6361/201424609

Khouri, T., de Koter, A., Decin, L., et al. 2014, Astronomy & Astrophysics, 561, A5, doi: 10.1051/0004-6361/201322578

Las Cumbres Observatory. Accessed 2022-01-27, Types of Stars. https://lco.global/spacebook/stars/types-stars/

Martin Pugh. 2018, Star Clusters. https://www.martinpughastrophotography.space/star-clusters

Massalkhi, S., Agúndez, M., Cernicharo, J., et al. 2018, Astronomy & Astrophysics, 611, A29, doi: 10.1051/0004-6361/201732038

McQuarrie, D. A. 2007, Quantum Chemistry (New York: University Science Books)

Meixner, M., Haas, M. R., Tielens, A. G. G. M., Erickson, E. F., & Werner, M. 1992, The Astrophysical Journal, 390, doi: 10.1086/171301

NASA. 2018, R Leporis: A Vampire's Star | Science Mission Directorate. https://science.nasa.gov/r-leporis-vampires-star

NASA JPL. Accessed: 2022-04-26, Galaxy Evolution Explorer - Universe Missions - NASA Jet Propulsion Laboratory. https://www.jpl.nasa.gov/missions/galaxy-evolution-explorer-galex

Physics & Universe. 2013, Harvard Spectral Classification. https://physicsanduniverse.com/harvard-spectral-classification/

Ramstedt, S., & Olofsson, H. 2014, Astronomy & Astrophysics, 566, A145, doi: 10.1051/0004-6361/201423721

Ramstedt, S., Vlemmings, W. H. T., Doan, L., et al. 2020, Astronomy & Astrophysics. http://arxiv.org/abs/2008.07885

Reimers, D. 1975, Memoires of the Societe Royale des Sciences de Liege, 8, 369–382

Rutten, R. J. 2003, Radiative transfer in stellar atmospheres (Institute of Theoretical Astrophysics Oslo: Sterrekundig Instituut Utrecht). https://robrutten.nl/rrweb/rjr-pubs/2003rtsa.book.....R.pdf

Rybicki, G. B. and Hummer, D.G. 1991, An accelerated lambda iteration method for multilevel radiative transfer, 171 – 181

Saberi, M., Maercker, M., Beck, E. D., et al. 2017, Astronomy & Astrophysics, 599, A63, doi: 10.1051/0004-6361/201629901

Saberi, M., Vlemmings, W. H. T., & De Beck, E. 2019, Astronomy & Astrophysics, 625, A81, doi: 10.1051/0004-6361/201935309

Salaris, M., & Cassisi, S. 2005, Evolution of Stars and Stellar Populations (Chichester, West Sussex, England: John Wiley & Sons, Ltd), 118–121

Splatalogue. 2022, SPLATALOGUE - FRAMES. https://splatalogue.online//advanced.php

Srinivasan, S., Meixner, M., Leitherer, C., et al. 2009, The Astronomical Journal, 137, 4810–4823, doi: 10.1088/0004-6256/137/6/4810

Takigawa, A., Kamizuka, T., Tachibana, S., & Yamamura, I. 2017, Science Advances, doi: 10.1126/sciadv.aao2149

Van de Sande, M., Sundqvist, J. O., Millar, T. J., et al. 2018, Astronomy & Astrophysics, 616, A106, doi: 10.1051/0004-6361/201732276

Vlemmings, W. H. T., Maercker, M., Lindqvist, M., et al. 2013, Astronomy & Astrophysics, 556, L1, doi: 10.1051/0004-6361/201321821

Weidner, C., & Vink, J. S. 2010, Astronomy & Astrophysics, 524, A98, doi: 10.1051/0004-6361/201014491

Wilson, T., Rohlfs, K., & Hüttemeister, S. 2013, Tools of Radio Astronomy; 6th ed. (Berlin Heidelberg: Springer-Verlag), 1–18, 145–185, 277–285, 319–328, 387–417

Wilson, T. L. 2018, Introduction to Millimeter/Sub-millimeter Astronomy, ed. M. Dessauges-Zavadsky & D. Pfenniger, Vol. 38 (Berlin, Heidelberg: Springer Berlin Heidelberg), 1–109, doi: 10.1007/978-3-662-57546-8_1

Wood, P. R. 2007, ASP Conference Series, 374. https://articles.adsabs.harvard.edu/pdf/2007ASPC..374...47W